Investigating Left Ventricle Wall Motion Using Cardiac Magnetic Resonance Imaging

By

Tareq Alrefae

Submitted to the Department of Physics and Astronomy and the Faculty of the Graduate School of the University of Kansas in partial fulfillment of the requirements for the degree of Doctor of Philosophy

_____
Mehmet Bilgen (Co-Chair)

_____
Larry T. Cook

_____
Chris Fischer

_____
Jack (JiCong) Shi (Co-Chair)

_____
Irina V. Smirnova

Date defended:_____

The Dissertation Committee for Tareq Alrefae certifies that this is the approved version of the following dissertation

Investigating Left Ventricle Wall Motion Using Cardiac Magnetic Resonance Imaging

Committee:

_____
Mehmet Bilgen (Co-Chair)

_____
Larry T. Cook

_____
Chris Fischer

_____
Jack (JiCong) Shi (Co-Chair)

_____
Irina V. Smirnova

Date approved:_____

Abstract

Magnetic resonance imaging (MRI) is an established radiological technique for assessment of cardiac function. Various MRI methods are utilized for global and regional evaluation of the myocardium through tracking the motion of tissue as the heart beats. Such tracking of motion reveals local as well as global deformation of the heart wall during contraction and relaxation. It has been shown that wall motion profiles of a healthy heart differ than those of a diseased heart due to variations in contractile behavior resulting from complications and abnormalities. Therefore, understanding heart wall motion and quantifying contractility serve as a valuable tool for evaluating myocardial viability as well as diagnosis of heart condition. Hence, in this presented work the focus is to utilize cardiac MRI techniques to develop computational algorithms that accurately describe myocardial motion in both global and regional aspects. Through acquiring cardiac MRI data from rat subjects, quantitative measurements are performed and mathematical models are formulated to quantify contractility and map local myocardial motion. Such measurements and formulations serve as means for providing important bio-imaging markers that reflect the state of the myocardial tissue, as well as indicators for inspecting the condition of the heart.

Table of Contents

Introduction

Cardiac Magnetic resonance imaging (MRI) is an established radiological technique for assessment of cardiac function in clinics. Particularly, tagged MRI methods allow for regional evaluation of the myocardium through generation of dark grid lines in acquired cardiac images. These dark lines, also known as tags, follow the motion of underlying tissue, as the heart beats, thereby revealing localized deformation of the heart wall. It has been shown that local wall motion profiles of a healthy heart differ than those of a diseased heart due to variations in contractile behavior resulting from complications like infarct, diabetes or stiff fibrotic tissue deposition. Understanding heart wall motion and quantifying contractility is therefore important to the evaluation of myocardial viability and the diagnosis of heart condition. This dissertation work is to develop a computational algorithm that utilizes MRI techniques to accurately the describe myocardial motion in both global and regional aspects. With MRI data from rat subjects, a mathematical model of the myocardial motion is formulated to quantify contractility and to map local myocardial motion. Such measurements and formulations provide important bio-imaging markers that reflect the state of the myocardial tissue, and could serve as clinical indicators for inspecting the condition of the heart. This dissertation is organized as follows. Chapter 1 introduces the basic physics of MRI. Chapter 2 discusses cardiac MRI methods that were used in this study. A novel model to describe cardiac wall motion from MRI data is introduced in Chapter 3. A time-reversal approach to estimate myocardial motion with MRI data is discussed in Chapter 4. Chapter 5 presents an

innovative method to measure the spin-spin relaxation time of MRI for a beating heart. In Chapter 6, image transformation techniques for the study of the motion of the heart's left ventricle are discussed. Finally, a graphical user interface (GUI) that enables users to apply image transformations that mimic cardiac wall motion is included in Appendix A.

CHAPTER 1: BASIC MRI PHYSICS

In this chapter the basic features of MRI are briefly discussed. The detailed treatment can be found in many references such as Ref [1].

Dynamics of a Single Spin in an External Magnetic Field

Most atomic nuclei possess spin angular momentum, a characteristic that enables them to interact with external magnetic fields [1, 2]. Such interaction is the basis of MRI. Spin, which is a pure quantum mechanical quantity, can be viewed as an angular momentum arising from rotation of the nucleus around an axis through its center. Hence, the nucleus spin is a vector oriented parallel to the axis of rotation with a magnitude given by

$$\left|\vec{S}\right| = \hbar\sqrt{I(I+1)} \quad , \hbar = \frac{h}{2\pi} \qquad (1.1)$$

where h is the Plank constant and I is the spin quantum number. Nucleus that is most commonly used in MRI is Hydrogen (^{1}H) with I = ½. With an external magnetic field $\vec{B}_0$, the projection of the spin vector in the direction of $\vec{B}_0$ is quantized as $S_z = m_I\hbar$, where m_I = -I, ..., I is the magnetic quantum number that represents 2I+1 orientations of a spin in the external magnetic field. The magnetic moment of a spin $\vec{S}$ is defined as

$$\vec{\mu} = \gamma\vec{S} \qquad (1.2)$$

where γ is the gyromagnetic ratio and equals to 42 MHz/T for ^{1}H. The magnetic energy of a spin in the magnetic field can be calculated as

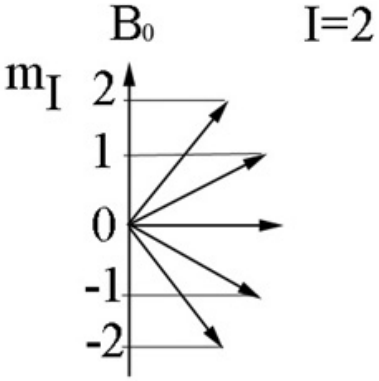

Figure 1.1: Quantization of the spin vector

$$E = -\vec{\mu} \cdot \vec{B}_0 \qquad (1.3)$$

which results in the quantized energy states of the spins,

$$E_{m_I} = -m_I \gamma \hbar B_0 \qquad (1.4)$$

The energy transition between two states can be expressed as

$$\Delta E = \hbar \omega \qquad (1.5)$$

where ω is the photon frequency of the radiation. For a transition between two adjacent states, the frequency is called the Larmor frequency $\omega_0 = \gamma B_0$. For ^{1}H, ω_0 = 420 MHz at B_0=10 T which is in the radio frequency (RF) range. With the interaction between $\vec{\mu}$ and $\vec{B}_0$, $\vec{\mu}$ tends to align with $\vec{B}_0$. Due to thermal fluctuations, however, $\vec{\mu}$ usually orients at an angle to and precesses around $\vec{B}_0$.

Macroscopic View

Consider an ensamble of nuclei of spin quantum number *I* in an external magnetic field $\vec{B}_0$ that is oriented in the z direction. Each spin has an energy of E_m given in Eq. (1.4). The equilibrium distribution of the spins is the Boltzmann distribution,

$$N_m = N_0 \frac{e^{-\frac{E_m}{k_B T}}}{\sum_{n=-I}^{I} e^{-\frac{E_n}{k_B T}}} \qquad (1.6)$$

where N_m is the number of spins in the energy state E_m, N_0 is the total number of spins, T is the temperature, and k_B is the Boltzmann constant. The magnetization of the ensamble of spins is

$$\vec{M} = \langle \vec{\mu} \rangle \qquad (1.7)$$

Because the external magnetic field is in the z direction, the transverse components of each $\vec{\mu}$ is randomly oriented in the transverse (*x-y)* plane and, thus $M_x = M_y = 0$. The longitudinal component M_z however, does not vanish. For nuclei with spin ½ such as ^1H, there are two spin energy states, spin up (m=½) and spin down (m=- ½), and the magnetization can be calculated from Eqs. (1.6) and (1.7) as

$$M_z = \frac{1}{2}\gamma\hbar N_0 \frac{e^{\frac{\gamma\hbar B_0}{2kT}} - e^{-\frac{\gamma\hbar B_0}{2kT}}}{e^{\frac{\gamma\hbar B_0}{2kT}} + e^{-\frac{\gamma\hbar B_0}{2kT}}} = \frac{1}{2}\gamma\hbar N_0 \cdot \tanh\left(\frac{\gamma\hbar B_0}{2kT}\right) \qquad (1.8)$$

For a field of B_0=10 T and at room temperature (~300 K), $M_z \sim 10^{-32} N_0 \quad J/T$.

For 1 mg of water, $N_0 \sim 10^{19}$ and $M_z \sim 10^{-13}$ J/T. Such a small M_z can be measured by using the induction principle (Faraday's law) in MRI.

Dynamics of Magnetization

In the presence of the external field $\vec{B}_0$, the equilibrium state of the magnetization of a biological sample is $M_x = M_y = 0$ and $M_z = M_{z0}$ where M_{z0} is given in Eq. (1.8). If the system is perturbed by another magnetic field, the magnetization will be away from the equilibrium. After the perturbation, the magnetization will relax back to the original equilibrium state. The relaxation process depends on the sample structure. In MRI, the characteristic of this relaxation is therefore measured for the information of the biological structure of the sample.

With only $\vec{B}_0$ in the longitudinal direction, the spins in a biological sample precess at a small angle around $\vec{B}_0$ with the Larmor frequency ω_0. To excite the spins, another magnetic field $\vec{B}_1$ that is perpendicular to $\vec{B}_0$ is applied in MRI. Under the perturbation of $\vec{B}_1$, the spins will tip away from $\vec{B}_0$ with a larger angle. In order to efficiently perturb the spins, the direction of $\vec{B}_1$ has to rotate with the spins. Note that $\vec{B}_1$ is much weaker than $\vec{B}_0$ ($B_1/B_0 \sim 0.1\%$). The rotational frequency of $\vec{B}_1(t)$ is therefore the same as the Larmor frequency.

To describe the dynamics of the excited magnetization of a sample, it is convenient to use a rotating reference frame in which $\vec{B}_1(t)$ is constant. Consider a spin that precesses around $\vec{B}_0$ in the clockwise direction (see Fig. 1.2). The transverse

plane (*x'-y'*) of the rotating frame rotates with the precession in the same direction with the Larmor frequency ω_0. The transformations between the rotating frame $(\vec{e}_{x'}, \vec{e}_{y'}, \vec{e}_{z'})$ and the lab frame $(\vec{e}_x, \vec{e}_y, \vec{e}_z)$ is then

$$\begin{aligned} \vec{e}_{x'} &= \cos(\omega_0 t)\vec{e}_x - \sin(\omega_0 t)\vec{e}_y \\ \vec{e}_{y'} &= \sin(\omega_0 t)\vec{e}_x + \cos(\omega_0 t)\vec{e}_y \\ \vec{e}_{z'} &= \vec{e}_z \end{aligned} \qquad (1.9)$$

In the lab frame, $\vec{B}_1(t)$ is in the transverse plane and is rotating with the spin as

$$\vec{B}_1(t) = B_1\left[\cos(\omega_0 t)\vec{e}_x - \sin(\omega_0 t)\vec{e}_y\right] = B_1\vec{e}_{x'} \qquad (1.10)$$

In the rotating frame, therefore, $\vec{B}_1$ is a constant field in the x' direction. Note that $\vec{B}_0$ is still in the longitudinal direction in both lab and rotating frames.

The dynamics of $\vec{M}$ in the presence of $\vec{B}_0$ and $\vec{B}_1(t)$ is governed by the Bloch equation

$$\frac{d\vec{M}}{dt} = \gamma\vec{M} \times \vec{B} \qquad (1.11)$$

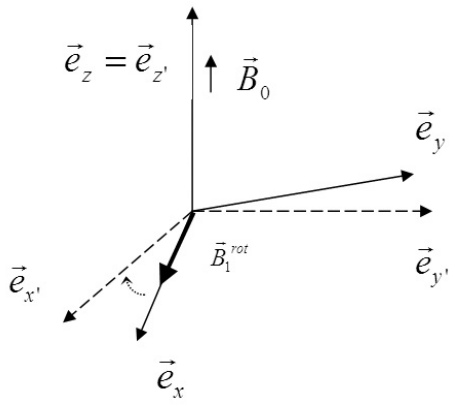

Figure 1.2: Lab and rotating frames.

In rotating frame, the time derivative of $\vec{M}$ can be written as

$$\frac{d\vec{M}}{dt} = \frac{\partial \vec{M}}{\partial t} + \vec{\Omega} \times \vec{M} \qquad (1.12)$$

where $\vec{\Omega} = -\omega_0 \vec{e}_{z'}$, $\vec{M} = M_{x'}\vec{e}_{x'} + M_{y'}\vec{e}_{y'} + M_z\vec{e}_z$ and

$$\frac{\partial \vec{M}}{\partial t} = \frac{dM_{x'}}{dt}\vec{e}_{x'} + \frac{dM_{y'}}{dt}\vec{e}_{y'} + \frac{dM_{z'}}{dt}\vec{e}_{z'} \qquad (1.13)$$

In the rotating frame, the Bloch equation becomes

$$\frac{d\vec{M}}{dt} = \gamma \vec{M} \times \left(\vec{B} + \frac{\vec{\Omega}}{\gamma} \right) \qquad (1.14)$$

where $\vec{B} = B_0\vec{e}_z + B_1\vec{e}_{x'}$. With the resonance condition of $\vec{\Omega} = -\gamma \vec{B}_0$, the Bloch equation in the rotating frame reduces to

$$\frac{d\vec{M}}{dt} = \omega_1 \left(\vec{M} \times \vec{e}_{x'} \right) \qquad (1.15)$$

where $\omega_1 = \gamma B_1$. Consider an initial condition of a typical MRI measurement in which $M_{x'} = M_x = 0$, $M_{y'} = M_y = 0$, and $M_{z'} = M_z = M_{z0} = 0$ at t=0. $\vec{M}(t)$ can be easily solved from Eq. (1.15) as

$$\begin{aligned} M_{x'} &= 0 \\ M_{y'} &= M_{z0} \sin(\omega_1 t) \\ M_{z'} &= M_{z0} \cos(\omega_1 t) \end{aligned} \qquad (1.16)$$

where M_{z0} is the maximum (longitudinal) value of the magnetization.

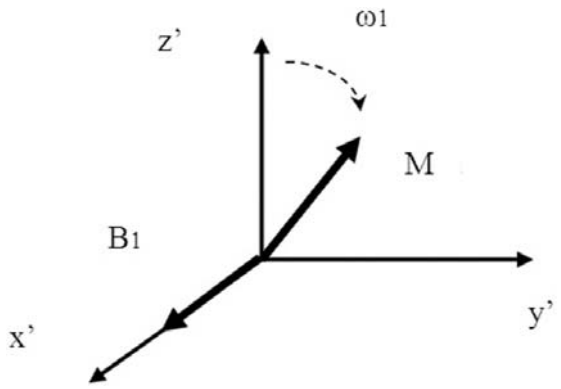

Figure 1.3: Precession of $\vec{M}$ around $\vec{B}_1$ in the rotating frame.

As shown in Eq. (1.16), $\vec{M}$ precesses around $\vec{e}_{x'}$ with angular velocity ω_1 in the rotating frame (see Fig. 1.3). In MRI, $\vec{B}_1(t)$ is usually applied as a pulse. For a pulse $\vec{B}_1(t)$ with a duration of Δt, the angle precessed (tipped away from $\vec{e}_{z'} = \vec{e}_z$) for $\vec{M}$ is $\theta_{\Delta t} = \omega_1 \Delta t = \gamma B_1 \Delta t$. In MRI measurement, a 90° tip is usually preferred for a strong signal. For B_1 ~10 mT, the duration of the pulse $\vec{B}_1(t)$ is about 2 ms.

Relaxation Mechanism

Consider the case of 90° tip in which $\theta_{\Delta t} = 90^\circ$ of $\vec{M}$ due to $\vec{B}_1(t)$. Right after $\vec{B}_1(t)$ is switched off, $M_x = M_{y'} = M_{z0}$, $M_y = M_{x'} = 0$, and $M_z = M_{z'} = 0$. After the switch-off $\vec{B}_1$, the restoration of $\vec{M}$ to its equilibrium ($M_z = M_{z0}, M_x = M_y = 0$) occurs via two dissipative processes. The first process is the release of the magnetic energy in the form of heat from the spins to the surrounding materials. This process

is directly linked to the alignment of $\vec{M}$ to $\vec{B}_0$ as M_z recovers from 0 to M_{z0}. The restoration of the M_z is governed by

$$M_z = M_{z0}(1 - e^{\frac{-t}{T1}}) \qquad (1.17)$$

where T_1 is the longitudinal relaxation time. The second restoration process of $\vec{M}$ is the randomization of M_x. After the switch-off of $\vec{B}_1$, M_x is gradually randomized from $M_x = M_{z0}$ to $M_x = 0$. During this process M_x is measured by a closely placed coil. This measurement is commonly referred as MRI signal. The decay of the MRI signal is therefore

$$M_x = M_{z0} e^{\frac{-t}{T2}} \qquad (1.18)$$

where T_2 is the transverse relaxation time. Typically

CHAPTER 2: CARDIAC MRI

The heart is an important organ which is in a continuous state of motion. Its non-stopping beating activity poses challenge to cardiac magnetic resonance imaging (CMRI) procedures. Nonetheless, the importance of the organ serves as a motivator for development and improvement of CMRI tools. Indeed, new CMRI techniques allow for obtaining images of high spatial resolution during a fraction of a cardiac cycle. Such treatment requires data acquisition during intervals that are short compared to characteristic time scales of cardiac motion. Such requirement necessitates routine use of electrocardiogram (ECG) triggering in CMRI practice. Moreover, other CMRI strategies are used depending on the particular application. This chapter discusses basic principles and tools of CMRI.

Motion Compensation

As introduced above, the high speed of cardiac motion is a source of artifacts in CMRI. In spite of widely used, fast MRI sequences, time scales of these imaging protocols are often inadequate for cardiac imaging [1]. Thus, approaches to compensate for motion are required to minimize motion-related artifacts. Consequently, combining motion-compensation techniques with imaging sequences form the basis of CMRI where the goal is to produce high quality, reliable data.

The idea of motion-compensation is borrowed from photography. When shooting a photograph of a rapidly moving object, long exposure would generally cause blurring. Thus, one approach would be to reduce exposure time such that the produced image is artifact-free. Nonetheless, cardiac motion remains too fast to be

captured in one exposure using the current available technology. Hence, the remedy is to divide a single exposure into several short exposures in what is known as k-space segmentation. This approach is done by utilizing the periodicity of cardiac motion where data acquisition is divided among multiple cardiac cycles. In our rat studies, we typically use 256 cardiac cycles where one k-space line of data is acquired per cycle. Thus, the outcome is a 256x256 snapshot image of the desired cardiac phase.

Experimentally, image acquisition is performed with ECG triggering, where the R peak (highest peak in the cardiac cycle) is used as a synchronizing signal (Figure 2.1). Thus, elements of the data matrix are gathered in consecutive cardiac cycles. For a given cardiac cycle, each act of gathering lasts for the duration of the acquisition window and is activated after the delay time with respect to the R peak elapses, thereby targeting a specific cardiac phase. To further enhance image quality, selection of a short acquisition window is recommended where fewer elements of the data matrix are gathered per cardiac cycle. It is noteworthy that such enhancement comes with the price of long scan times, since a typical scan time is a function of duration of acquisition window per cycle and the number of cycles involved.

Because breathing motion adds complications, only cardiac cycles that are away from rapid respiratory movement are considered for imaging. Hence, monitoring of respiration signal is required, especially for animal experiments where breath-hold is not possible. Figure 2.2 shows a snapshot of ECG and breathing monitoring of CMRI experiment performed on a rat subject. With the selected

settings in Fig 2.2 where the respiratory window acquisition (250 ms) was chosen to be close to the cardiac period (210 ms), about one cardiac cycle is considered for imaging per respiratory cycle. Thus, for a respiration period of 1940 ms, a 256x256 cardiac image takes about eight minutes to produce.

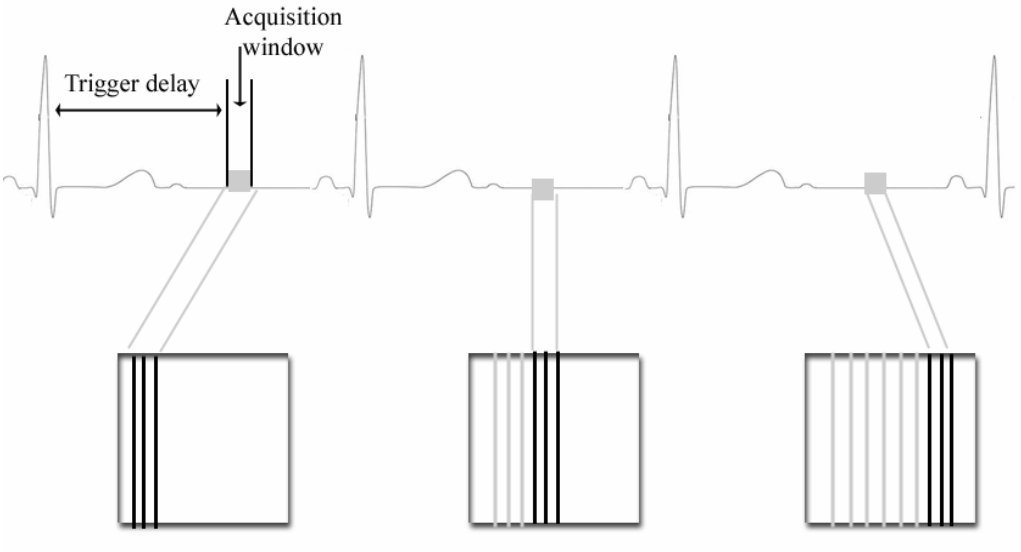

Figure 2.1:
Periodicity of cardiac motion is utilized with ECG triggering. Acquisition window starts after trigger delay time elapses with respect to the R peak. Collection of the elements of the data matrix lasts for the duration of the acquisition window per cycle.

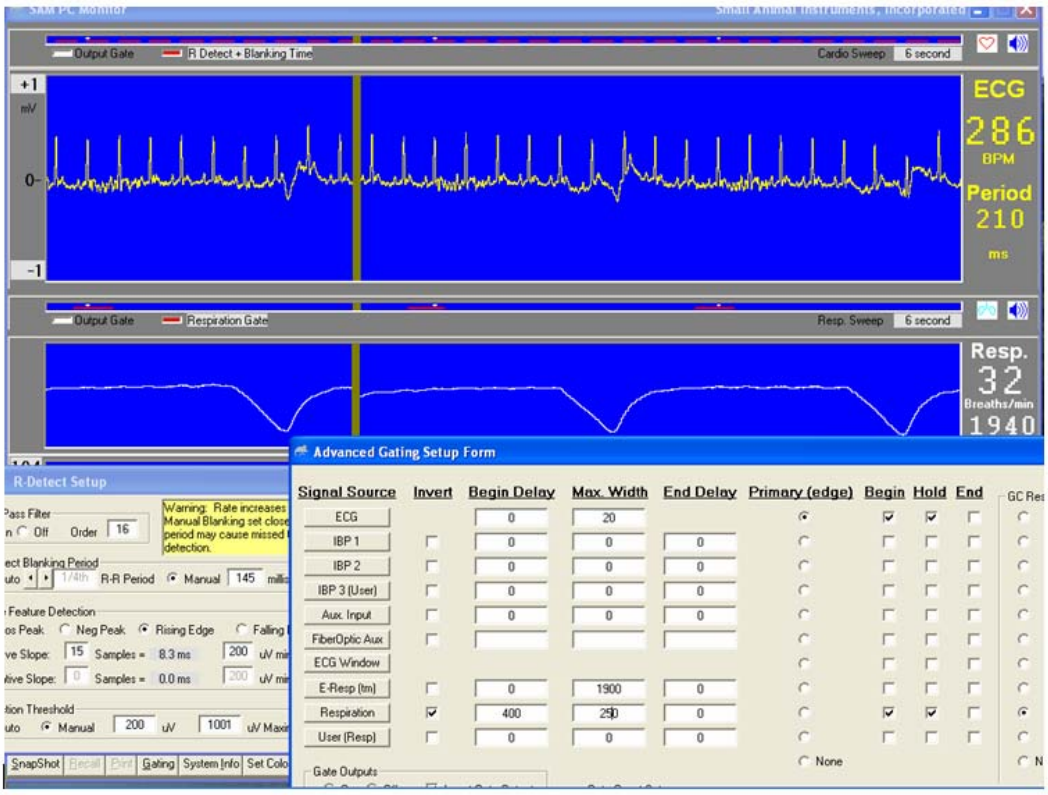

Figure 2.2:
Screen snapshot of ECG and respiration monitoring system taken at a CMRI experiment on a rat subject. The ECG wave has a period of 210 ms, and the respiratory wave has a period of 1940 ms. Acquisition window for cardiac signal was set to 20 ms with 0 ms delay (to capture the end diastole as the first phase in the sequence of images). For respiration, acquisition window was set to last for 250 ms after a delay of 400 ms that starts right after minimum point (dip). These settings ensure data gathering in the plateau of the respiration signal and away from rapid breathing motion.

Cine and tagged imaging

During a typical cardiac cycle, the myocardium goes through various phases with complex behavior. To observe such rapid changes, it is important to monitor myocardial motion throughout the cardiac cycle. In general, cine imaging is the approach of choice to study movement exhibited by the heart [1]. Cine imaging employs ECG triggering and k-space segmentation to gather multiple data sets corresponding to various cardiac phases. The result is a set of sequential images that could be viewed as a movie, hence the term cine (short for cinema). Figure 2.3 shows an illustration of cine imaging with two phases per cycle. It is certainly possible to fill the available time in each cycle with distinct images to obtain a better description of the behavior in myocardial motion.

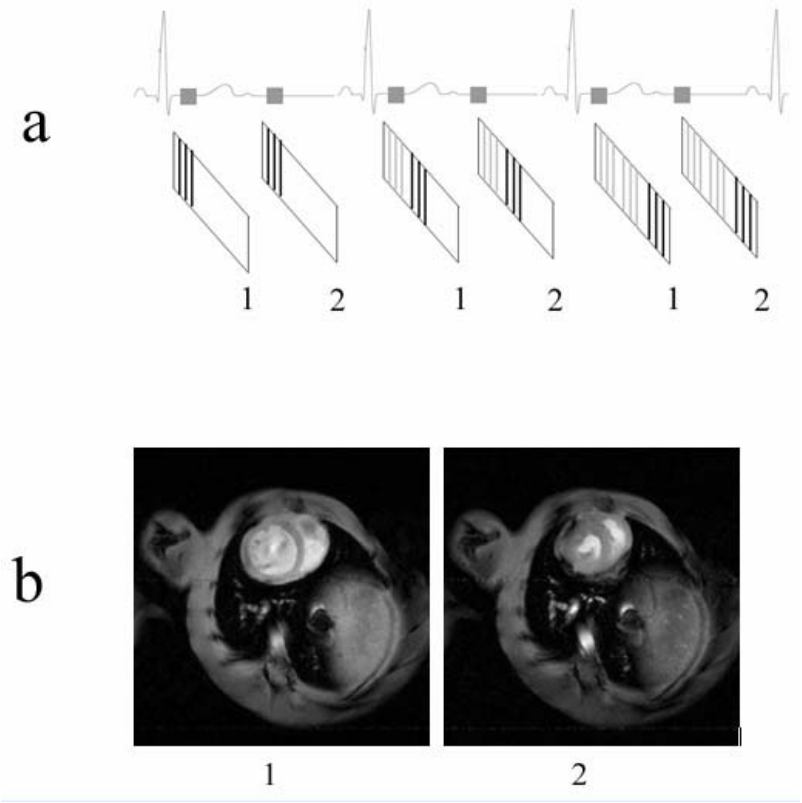

Figure 2.3: An illustration of cine imaging is shown in (a) with two phases per cycle. The two acquired images are shown in (b), end diastole and end systole.

Using cine imaging by itself is good to study global variation in myocardial motion. To study regional variation, however, cine imaging is combined with tagging to yield grids of saturated magnetization that follow the motion of underlying tissue [1]. These grids are formed through a technique known as Spatial Modulation of Magnetization (SPAMM) [4-7]. Through application of RF pulses, SPAMM places tag lines, which make series of parallel and/or orthogonal stripes on the slice being imaged. Typically, a SPAMM pulse consists of two RF pulses with a magnetic field gradient lobe sandwiched in between (Figure 2.4). Assuming both RF pulses have a flip angle of 90 degrees and are applied along the *x* axis in the rotating reference frame, Figure 2.5 provides a qualitative description of the tagging process. The first

RF pulse tips the magnetization vector to the transverse plane (Fig. 2.5 a). Then the tagging gradient is applied which causes phase dispersion in the transverse magnetization (Fig. 2.5 b), where the degree of dispersion depends on spatial location along the gradient direction. After that, the second RF pulse is applied which causes the transverse magnetization to rotate 90 degrees about the *x* axis, transferring the magnetization from the *xy* plane to the *xz* plane (Fig. 2.5 c). The transverse component of magnetization will continue to disperse until it dies out, while the longitudinal component survives due to the external magnetic field $\boldsymbol{B_0}$. Hence, the magnitude of the magnetization vector will depend on its spatial location $M_z(r)$, and thus a modulation of magnetization is produced.

Observing the tagging process quantitatively, after the first RF pulse (Figure 2.5 a), magnetization in the rotating reference frame could be described as:

$$\begin{bmatrix} M_x \\ M_y \\ M_z \end{bmatrix} = M_0 \begin{bmatrix} 0 \\ \sin\theta_1 \\ \cos\theta_1 \end{bmatrix} \qquad (2.1)$$

where M_0 is the equilibrium value of magnetization, and θ_1 is the flip angle of the first RF pulse. Thus, application of the tagging gradient G_{Tag} introduces a spatially dependent phase to the transverse magnetization

$$\varphi(r) = \gamma \cdot r \int_0^T G_{Tag}\, dt \qquad (2.2)$$

where r is a spatial variable along the gradient direction, γ is the gyromagnetic ratio, and T is the duration of G_{Tag}. Phase dispersion causes magnetization to become

$$\begin{bmatrix} M_x(r) \\ M_y(r) \\ M_z \end{bmatrix} = M_0 \begin{bmatrix} \sin\theta_1 \sin\varphi(r) \\ \sin\theta_1 \cos\varphi(r) \\ \cos\theta_1 \end{bmatrix} \qquad (2.3)$$

After the second RF pulse is applied, magnetization vectors rotate about the x axis

$$\begin{bmatrix} M_x(r) \\ M_y(r) \\ M_z \end{bmatrix} = M_0 \begin{pmatrix} 1 & 0 & 0 \\ 0 & \cos\theta_2 & \sin\theta_2 \\ 0 & -\sin\theta_2 & \cos\theta_2 \end{pmatrix} \begin{bmatrix} \sin\theta_1 \sin\varphi(r) \\ \sin\theta_1 \cos\varphi(r) \\ \cos\theta_1 \end{bmatrix} \qquad (2.4)$$

where M_x and M_y dephase and die out, and only M_z survives

$$M_z(r) = -M_0[\sin\theta_1 \sin\theta_2 \cos\varphi(r) - \cos\theta_1 \cos\theta_2] \qquad (2.5)$$

which is spatially modulated by $\cos\varphi(r)$. Hence, images acquired subsequently will have tags that act as if they were attached to underlying tissue (Figure 2.6).

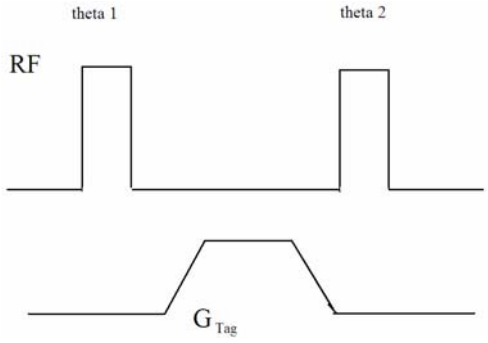

Figure 2.4:
RF pulses with flip angles, and tagging gradient lobe sandwiched in between.

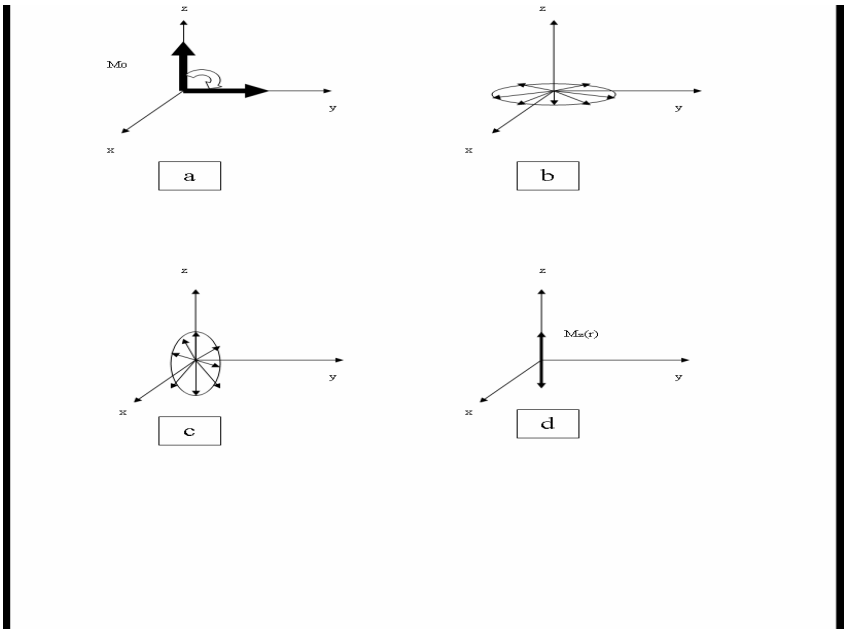

Figure 2.5: Evolution of magnetization during SPAMM which leads to formation of tags.

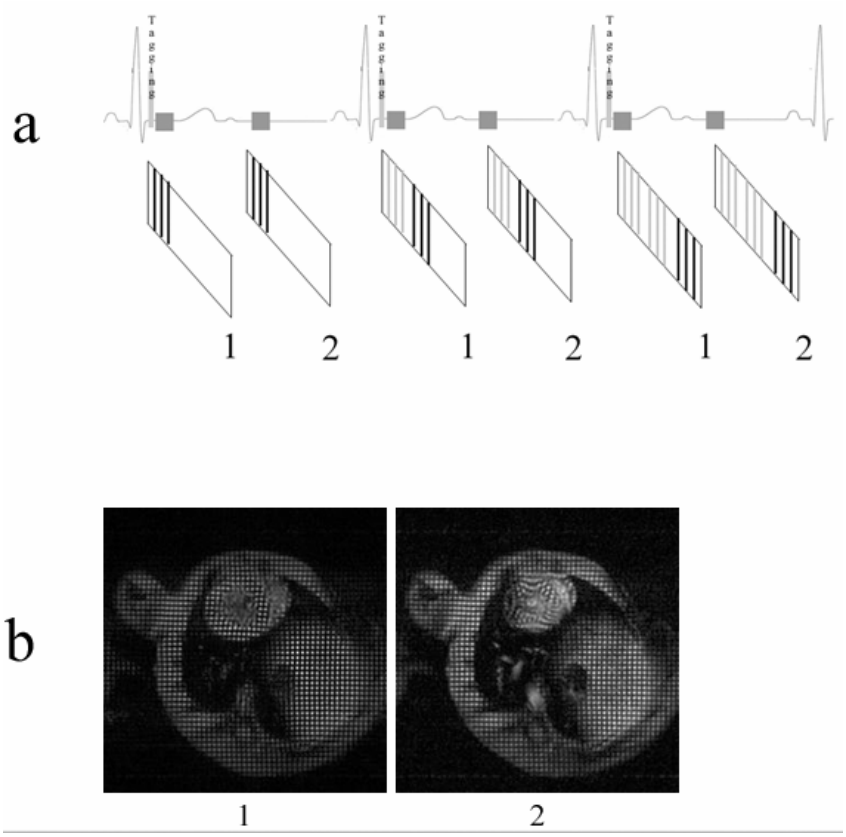

Figure 2.6:
An illustration of tag-cine imaging is shown in (a) with two phases per cycle. Notice the tagging sequences are applied right after the R-peak before data acquisition. The two acquired images are shown in (b), end diastole and end systole.

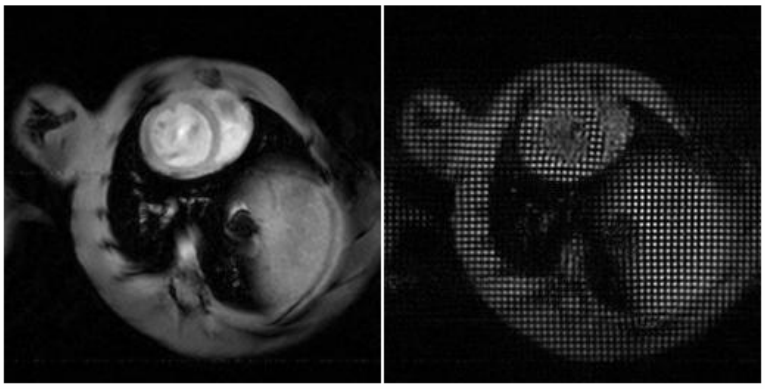

Figure 2.7:
A Cine image (left) and tag-cine image (right).

CHAPTER 3:
PART I
A simple time-dependent model of left ventricle motion - implementation using tagged MRI

This chapter consists of the manuscript submitted for peer review prior to publication. It essentially discusses a model that describes motion of the left ventricle during systole.

Chapter Summary

Background: Spatiotemporal modeling of myocardial motion is an active area of research. Its importance arises from the insights provided by the models that help understand and evaluate cardiac function. A valuable tool in model building efforts is the *in vivo* magnetic resonance imaging (MRI). This paper uses a tagged MRI data to construct a time-dependent model of the motion of the left ventricle (LV) at the mid-ventricular level in the short-axis view.

Methods: Theoretical analysis involved imposing assumptions with regard to the systolic motion of the LV. These assumptions were used to construct a Gaussian-based spatial transformation to describe the myocardial motion. Experimentally, cardiac tagged MRI data were gathered from five rats. Four of the rats were normal and one was diabetic with cardiomyopathy. The data were processed offline to segment the LV in a systematic and consistent manner. An algorithm was described to characterize the LV size and shape at different systolic phases using a realization of the Gaussian transformation.

Results: The Gaussian transformations were computed from the experimental tagged MRI data for normal and diabetic rats. The transformation for the diabetic rat was substantially different than the normative measurements, indicating the sensitivity of the model to detect an abnormality in the cardiac condition.

Conclusion: The one-parameter simple Gaussian model described in this paper provides a new way to characterize the LV wall motion. The motion measurements

made with this model allow evaluating the cardiac function and interpreting the viability of the myocardial tissue.

Key words: magnetic resonance imaging, tagged MRI, cardiac modeling, left ventricle, left ventricular wall motion.

Introduction

Cardiac dysfunction is associated with a variety of cardiovascular diseases that lead to heart failure. Significant cardiac events such as those in infracted or diabetic hearts are associated with the impaired relaxation and contraction of myocardium or abnormalities in left ventricular (LV) wall motion [1, 8]. Tagged magnetic resonance imaging (MRI) is an established cardiac imaging modality that is used to detect these regional conditions in both clinical and experimental studies [9-11]. Applications of this imaging technique have proved to be feasible and diagnostically valuable in evaluating the performance of normal or diseased hearts in live subjects using conventional global and regional measures [4-7, 12, 13].

Tagged MRI employs electrocardiogram (ECG) gated acquisition. The imaging sequence contains initial saturation pulses followed by a repetitive image acquisition [1]. At a specific time between the QRS peaks of the ECG waveform, spatial modulation of magnetization pulses is applied to saturate the spins perpendicular to the imaging plane in the body. Then, a series of images is acquired repetitively in equal time intervals covering the whole period of the heart beat. The resulting images provide snapshot views of the heart along either its short axis or long axis at different phases of the cardiac cycle. Depending on the nature and orientation of the saturation pulses, the first image in the series contains dark parallel lines, known as tags, which may be organized in horizontal, vertical or in both directions in a grid fashion. In the grid organization, the tags define boundaries of individual cells. Thickness and separation of the tag lines are set to desired values prior to the initiation of the data

acquisition. As the heart contracts or relaxes, the tags follow the motion of the underlying myocardial tissue. The degree of the deformation experienced by each tag cell provides a sensitive measure of regional motion and can be used to assess the viability of the myocardium within the cell volume.

Current research efforts are focused on spatiotemporal modeling of the LV shape and motion [8]. To aid these efforts, this paper introduces a mathematical construct as a means of quantitatively describing the LV wall motion in a beating heart using tagged MRI data. After providing a physical basis for supporting its construction and giving the details of its implementation, we test the sensitivity of the model built with data from normal hearts to detect the myocardial alterations in a diseased heart. In the accompanying paper (Part II), we demonstrate how the proposed motion model can be used to improve the computer-aided motion and regional deformation measurements by minimizing the errors made during the numerical estimation of the myocardial displacements.

Theory – Model of the LV wall motion in the short-axis view of the heart

Anatomical and structural characterization of the LV

For clinical analysis or evaluation purposes, the short axis view of the heart is divided into three sections, namely base, mid-ventricle and apex. This division is in accordance with the standardized myocardial segmentation published by the American Heart Association [11]. To perform its pumping task, the LV and its myocardial fibers are organized in a complex architecture both anatomically and structurally within these three levels [10]. As a result, the LV wall twists with respect

to its long axis at the base and apex in opposing directions, and consequently the deformations at these levels are governed by torsion together with a combination of radial and circumferential strains. The motion at the mid-ventricular level, on the other hand, is relatively twist-free and hence the deformation in this region is described mainly by the radial and circumferential strains. Moreover, the patterns and degrees of the LV wall motion are also known to depend on the size of the ventricle at the level observed. At the level of the mid-ventricle, the LV cavity diameter experiences its greatest radial shortening (elongation) during the systolic (diastolic) phase. If all aspects of the LV motion are considered, prior knowledge and experimental observations suggest that its complete characterization with a model would be a challenging task to undertake. Nevertheless, if the mid-ventricle is chosen as the specific level of interest, a simple yet powerful model can be constructed as discussed below. Due to the minimal torsion effects at the mid-ventricle, we propose a model that is capable of describing the LV wall motion comprehensively at this almost twist-free level.

Before proceeding further, we make the following basic assumptions for constructing the model to properly represent the LV motion at the mid-ventricle.

1) Constraints imposed on the myocardial tissues have negligible mechanical effects. For example, the LV tissues attached to the chest wall deform in the same manner as those attached to the septum.

2) Although a full cardiac cycle includes both systolic and diastolic phases, to keep the analysis simple, the model is built to mimic the systolic LV motion only, as

in [9]. Nonetheless, it is straightforward to extrapolate the analysis to include the diastolic phase if desired. The digital cardiac images acquired sequentially in equally spaced time intervals in the systolic phases are identified by the frames F_i for i=1,2…L, where i=1 is the end diastole frame and i=L is the end systole frame.

3) The cardiac images are constructed on a virtual canvas with rubber sheet properties that can be digitally stretched according to a spatially varying deformation pattern. With this elastic feature, the canvas serves as a basis upon which the model acts through the application of a spatial perturbation in the coordinates of the myocardial tissue. Thus, such a spatial transformation describes the local myocardial motion. As shown below, the canvas' elastic behavior is exploited through the use of time-forward operations applied on the images to simulate the real myocardial motion.

Physical Basis of the LV motion model

The mathematical basis for modeling the LV motion in the current work is an extension of the approximations employed in physical sciences. Such approximations are typically chosen to simplify otherwise complex, intractable problems representing physical phenomena. For example, quantum wells are used in solid state physics to understand the distribution of the electron density in spatially confined potentials [2]. Similarly, gravitational wells are used in astrophysics to represent gravitational forces of large masses acting on smaller bodies to shape their orbits [14]. Hence, analogous to these cases, we approximate the LV systolic motion at the mid-ventricle with a well that is shaped by a two-dimensional Gaussian profile chosen symmetric in

angular and radial directions to map the transverse section of the heart. Besides being simple and well understood, the Gaussian function has found wide-spread applications in many scientific fields. In the current application, the Gaussian function is used for deforming the image canvas to simulate the forward systolic motion of the LV wall during the cardiac cycle. The resulting effect by such deformation is equivalent to shifting the image coordinates under a spatially variant affine-like transformation, thereby making the transformed state resemble the myocardial contraction observed during the systole. Mathematically, the motion model can explicitly be expressed by the coordinate transformation **T** defined by

$$\mathbf{T} = \begin{pmatrix} 1 + e^{\frac{-(x^2+y^2)}{\alpha^2}} & 0 \\ 0 & 1 + e^{\frac{-(x^2+y^2)}{\alpha^2}} \end{pmatrix}. \tag{3.1}$$

Here x and y represent spatial coordinates. The parameter α in the exponent is responsible for the amount of radial deformation applied on the canvas, and is therefore time dependent when the serially-acquired image frames are considered. The real cardiac tagged MRI data are used to estimate α_i in characterizing the LV motion from the first frame i=1 ($\alpha \rightarrow 0$) to a selected frame I_i, i=2,3…L, as described below. Figure 1 illustrates the application of this transformation to canvases of two tagged images. A uniform image $I_1(x,y)$ in Fig. 1-a is labeled with regular grid tags. The operation $\mathbf{T}[I_1(x,y)]$ yields the deformed image $I_2(x,y)$ in Fig. 1-b, where the shape and size of the tag cells depict regional motion. If a donut-shaped disk in Fig. 1-c is used to mimic the LV wall, Fig. 1–d show the resulting deformed disk. The

radial LV wall motion is directly related to the value of α; small α yields small wall motion and large α produces large wall motion.

To accurately describe the myocardial motion, it is necessary to satisfy two main criteria observed in the MR experimental data and discussed in the literature [9]. First, the transformation function should exhibit radial dependence, so that image coordinates closer to the LV cavity's center are deformed more than those further away from the origin. This criterion is clearly satisfied in Figs. 1-b and 1-d. The bow-shaped behavior exhibited by the deformed lines indicates that the resulting deformation has radial dependence. Second, the transformation function causes an increase in the thickness of the LV walls, and a decrease in the size of the LV cavity as observed in the real systolic cardiac motion. This requirement is also met by the Gaussian model. The resulting donut in Fig. 1-d clearly exhibits increase in the wall thickness, and decrease in the cavity size, which are both desired features to accurately model the LV motion. In these regards, the parameter α alone can be seen as capable of mimicking the changes in the LV wall's diameter and thickness.

Methods and Procedures

Tagged MRI Acquisition

Cardiac MRI data from the mid-ventricle level were collected from five male Sprague-Dawley rats. Four of the rats were normal and the remaining one was made

diabetic with the procedures described previously in [15]. The rats were anesthetized using 1.5% isofluorane in a mixture of air and oxygen (60% and 40%, respectively) and scanned using a 9.4 T horizontal bore scanner (Varian Inc., Palo Alto, CA) and 60 mm radio frequency volume coil. ECG gated gradient echo based tagged images were captured from the short-axis view of the heart. The cardiac cycle was temporally resolved into ten equally incremented phases. The first five were the systolic frames. The following settings were used for the image acquisition: TR/TE = 25/2.44 ms, number of averages = 1, field of view = 60 x 60 mm, image matrix = 256 x 256, slice thickness = 2.0 mm. The square grid tags had dimensions of width = 0.3 mm and separation = 0.8 mm. All experimental procedures were approved by the University of Kansas Medical Center Institutional Animal Care and Use Committee.

Processing of Tagged MRI Data

Prior to performing the LV motion modeling, a set of image processing routines was implemented. The main task of these routines was to ensure that the resulting model was generic enough to either represent the myocardial motion in different species or account for the variations seen in the heart volumes within the same species under normal or pathological conditions. Application of this procedure aimed to segment out a portion of the acquired tagged image to visualize the LV in a larger short-axis view at the mid-ventricle. This segmentation process is given in detail in Fig. 3.2. As shown algorithmically in the figure, the end-diastole image, which was acquired when the LV is fully open as the first image of the systolic phase, was displayed on the computer screen. Next, four points that were 90 degrees apart were

selected on the outer circumference of the LV wall. Then, two crossing lines, each passing through two of the selected points, were drawn. The cross point of the two lines was set to represent the center C of the LV. The average of the lengths of the two lines was used as a measure of the LV diameter D. Next, a square window with equal size D in each dimension and centered at C was drawn to distinctly enclose the LV wall. A second concentric square window was applied with a slightly larger dimension $N = 1.3*D$ to extract a broader region containing the LV wall of the heart and the surrounding tissue mass. This last window was also used to segment out the LV from the remaining systolic image frames F_i for i=2,3…L. Finally, the extracted images from all frames were interpolated to an increased dimension of 256 x 256 pixels to obtain the final systolic image set I_i for i=1,2…L. Figure 3.3 shows a set of images obtained after the application of this segmentation routine followed by a spatial scaling of the image coordinates. With this standardization outlined and depicted in Fig. 3.2 as a flowchart, the displacement measurements are now expressed in terms of the pixel units.

Construction of the LV motion model using the spatial Gaussian transformation

The experimental data from each animal were preprocessed separately by following the algorithm described in Fig. 3.2 using all systolic frames. For modeling the forward LV motion, the resulting images were further analyzed to empirically find an optimal value for the deformation parameter α_i in Eq. (1) for each systolic

image frame I_i for i=2…L. This process involved superimposing a computer generated grid of binary grid mesh, on the LV image as described by the algorithm in Fig. 3.4. The forward transformation in Eq. (3.1) was applied to the undeformed mesh structure with a preselected α_{i0} value to deform the grid lines to match the tag lines in the image I_i as close as possible. Next, an iterative optimization procedure was implemented using a computer to achieve a best match by varying the parameter α_i. This procedure involved converting the LV image I_i to a binary form by applying an intensity threshold. The tag lines on the resulting image assumed zero intensity. Next, we performed a logical XOR operation between the binary image and the deformed grid mesh. The outcome of this operation in each position was 1 if the two pixel values were different, and 0 if they were the same. The results at pixels where the grid lines were collocated were summed. This sum was then normalized with the total number of pixels occupied by the lines on the grid mesh. A perfect match between the grid lines and the real tag lines would ideally produce a zero sum. This computational procedure was repeated for ten α_i values distributed between a range divided in equal intervals; $0.9*\alpha_{i0} < \alpha_{ij} < 1.1*\alpha_{i0}$, j=1…10. The value of α_{ij} producing the minimal normalized sum was selected as the optimal value for the deformation parameter α_i for the frame i. When the normalized sum attained the same value for more than one α_{ij}, we made a selection by visually inspected the matches on the computer screen. Figure 3.5 illustrates the deformed grids (in red) superimposed on top of all four tagged images acquired serially during the systole.

Results and Discussion

This study was initiated to seek a simple, yet comprehensive model with a sufficient number of elements to accurately represent the LV wall motion. With a set of basic assumptions and simplifying approximations, we proposed the Gaussian transformation in Eq. (3.1) to model the myocardial motion at the mid-ventricle level during systole. We specifically targeted the mid-ventricle for modeling because the minimal amount of torsion and twisting experienced by this level during the heart beat allowed building the model to account only for the radial motion of the LV. We empirically constructed the model parameters using real tagged MRI data gathered from rat hearts. This implementation involved data processing steps, which were described algorithmically in Figs. 3.2 and 3.4. The initial step involved windowing and scaling the images to consistently depict the LV size and shape with the same dimensions at the end-diastole. This approach made the model versatile enough to analyze the LV motion in different species or minimize the inter-variation of the measurements when the same species is considered. This feature of the model increases its capacity by simulating the LV motion in both humans and animals. The model is therefore plausible to use in clinical or experimental studies aimed at measuring cardiac performance to assess the efficacy of a drug treatment [16, 17] or to describe the role of exercise in delaying heart failure in diabetic cardiomyopathy, a deficiency of heart function caused by diabetes [18].

Irrespective of whether the data is clinical or experimental, our Gaussian LV model requires estimating a single deformation parameter α for quantifying the

temporal motion in the systolic phase of the cardiac cycle with sufficient accuracy. Requiring only one parameter to reasonably describe the myocardial deformation is another important feature of this model. Table 3.1 presents estimates for α with tagged MRI data obtained from the four normal rats used in the current study. The values are also plotted against the frame numbers in Fig. 3.7. In light of the data presented in the figure, α increases with time in a nonlinear fashion to accommodate the shrinkage of the LV size during the systolic contraction. These α values at different time points establishes a normative database which can be used as a reference for the comparison of results from tagged MRI experiments preformed on rats with abnormal cardiac conditions. In order to demonstrate this point, we scanned a rat with a diabetic history of four weeks duration and estimated an α for each systolic frame of the acquired data. As illustrated in Fig. 3.7, the values of α for the diabetic rat were considerably different from those of the normal rats. This difference is directly related to the variations in myocardial contraction between the two groups, which is attributed to the diabetic cardiomyopathy [15, 18-20]. In diabetic hearts, the myocardium loses its ability to contract efficiently due to fibrotic tissue depositions in the LV wall. The measurements of the deformation parameter α in our model can potentially be used to sensitively detect structural and functional changes in myocardial tissue early on or follow the progression of a disease longitudinally. In this regard, this parameter may offer a new biomarker not only in experimental studies but also in clinical applications.

Our model is also open to other clinical relevance. For example, strain calculation and its relation to the parameter α is a good area for future exploration in cardiac imaging research. Such a relation could, in principle, indicate a certain systolic dysfunction associated with certain diseases or abnormalities, such as diabetes as demonstrated above. Similarly, another useful parameter well accepted by clinicians is the myocardial strain rate. By calculating the differences in strains exhibited by the LV tissues from one systolic phase to another, more insights can be gained regarding myocardial behavior and its time dependence. Thus, investigating these and other potential merits of the Gaussian motion model of the LV are left for future work.

From another aspect, knowledge of the α values in Table 1 plays a role in applications where projecting the LV motion forward in time is required. By time-interpolating the α values, one can reconstruct simulated pseudo images corresponding to a specific time point chosen within the systolic phase of the cardiac cycle. These computational processes can be carried out offline by applying the transformation **T** in Eq. (1) to the canvas of the end-diastole image frame i=1 with the desired α value. Sample results from such computations are shown in Fig. 3.6, where the simulated pseudo images are presented with their experimental real time counterparts.

When reverse projection of a systolic frame in time is desired, the α values in Table 1 can be valuable in undoing the forward myocardial motion in systole. Briefly stated, this can be achieved by the inverse of the transformation **T** in Eq. (3.1). $\mathbf{T}^{-1}$ is

mathematically equivalent to setting up a time-reversal operator. Applying $\mathbf{T}^{-1}$ on the image frame I_i after substituting by α_i produces a simulated pseudo image that closely resembles to the end-diastolic image I_1. The ability to invert the motion in a mathematically well-defined fashion has important implications in reducing the errors made in quantifying the regional myocardial motion, especially when the displacements are large. The time-reversal operator $\mathbf{T}^{-1}$ and its capabilities are the subject of the accompanying paper (Part II) and its merits are further discussed in detail therein with examples.

Despite its ability to describe myocardial forward motion, our model suffers from two main limitations. The first limitation is that the model treats the entire myocardium as though it were contracting homogeneously. While such treatment greatly simplifies the problem, it completely ignores the heterogeneous nature of myocardial contractility. Evidently, contractility varies with the position of the myocardium such that tissues attached to the chest wall, for example, exhibit deformation profiles that differ from those of the septum. This variation in deformation is due to the fact that, depending on the location, some tissues have constraints that limit their motion while others do not. Accommodating this behavior of regional dependencies requires more complicated models for better description of the myocardial motion.

Another limitation of the model is its inability to handle twisting motion that takes place in the basal and apical levels. Thus, the model is limited to work at the mid-ventricle level where twist is minimal. Nonetheless, adding a twisting ability is

plausible and computationally possible by having position-dependent angles to account for rotation in the transform operator in Eq. (3.1). Such improvement may help the model describe myocardial motion at various levels of the LV in short axis views.

Although a typical cardiac cycle is composed of both systolic and diastolic phases, we chose to focus the model on systolic motion only. This approach was chosen to simplify the problem, knowing that we could easily extrapolate the analysis to include diastolic motion if desired.

A quick literature search reveals numerous approaches to modeling LV motion [8]. Examples include techniques based on finite elements [9], finite differences [21], B-spline methods [22] and prolate spheroidal basis functions [23]. Such techniques, along with others [8], have attained good results in describing the cardiac wall motion and computing useful clinical data like displacement and strain profiles. Nevertheless, to accurately describe the LV wall motion, these models require large numbers of parameters and intense numerical computations. The need for a simple, yet reliable model has therefore been met by the current implementation.

In summary, we presented a simple Gaussian model with a single parameter to describe the systolic LV motion. The model utilized a set of assumptions to simplify an otherwise complicated myocardial motion profile. Simplifications included introduction of a unique concept - an elastic image canvas with rubber sheet properties - upon which perturbations were performed digitally. The idea of spatially perturbing the canvas with a well was borrowed from other physical sciences and

accommodated to fit our requirements in modeling the changes in the shape and size of the LV wall. Our model consists of a simple spatial transformation operator that deforms the canvas in a Gaussian fashion. We showed that the radial time-forward motion of the LV at the mid ventricle level can reasonably be represented by this model and the model parameter is sensitive to the cardiac condition. In spite of the model's simplicity, the major potential of the model can be revealed when it is used in time-reversal mode while measuring cardiac function and output as demonstrated in the second paper (Part II).

Figure Captions

Figure 3.1. A uniform image $I(x,y)$ in Fig. 1-a is labeled with regular grid tags. The operation $\mathbf{T}[I(x,y)]$ yields the deformed image in Fig. 1-b, where the shape and size of the tag cells depict regional variations in motion. Similarly, a donut-shaped disk in Fig. 1-c is used as a simple model of the LV. Fig. 1–d shows the resulting deformed disk.

Figure 3.2. Algorithm describing the segmentation of the LV from a larger tagged image.

Figure 3.3. Segmented serial images (1-5) of the LV resized to 256x256 pixels during systole.

Figure 3.4. An algorithm to estimate an optimal value for the parameter α in the Gaussian transformation **T** using an image acquired at a systolic phase.

Figure 3.5. Real time systolic images (2-5) of the LV from Fig. 3. Superimposed is a grid (red) that was deformed offline using the Gaussian transformation **T** applied on the image 1 according to the algorithm in Figure 4. The grid (red) mimics the deformed tag lines in the underlying myocardial tissue. The estimated optimal α values are respectively 12, 16, 19 and 20.

Figure 3.6. Real and simulated pseudo images in systole. The simulated images were obtained offline using the operation **T** on the real tagged image 1 with the optimal α values 12, 16, 19 and 20, as in Fig. 5.

Figure 3.7. The deformation parameter α is plotted against the systolic image numbers, which are directly proportional to the acquisition time in the systolic phase. The curves in the graph show the results from the normal (n=4) and diabetic (n=1) rats.

Figure 3.1

A uniform image $I(x,y)$ in Fig. 1-a is labeled with regular grid tags. The operation $\mathbf{T}[I(x,y)]$ yields the deformed image in Fig. 1-b, where the shape and size of the tag cells depict regional variations in motion. Similarly, a donut-shaped disk in Fig. 1-c is used as a simple model of the LV. Fig. 1–d shows the resulting deformed disk.

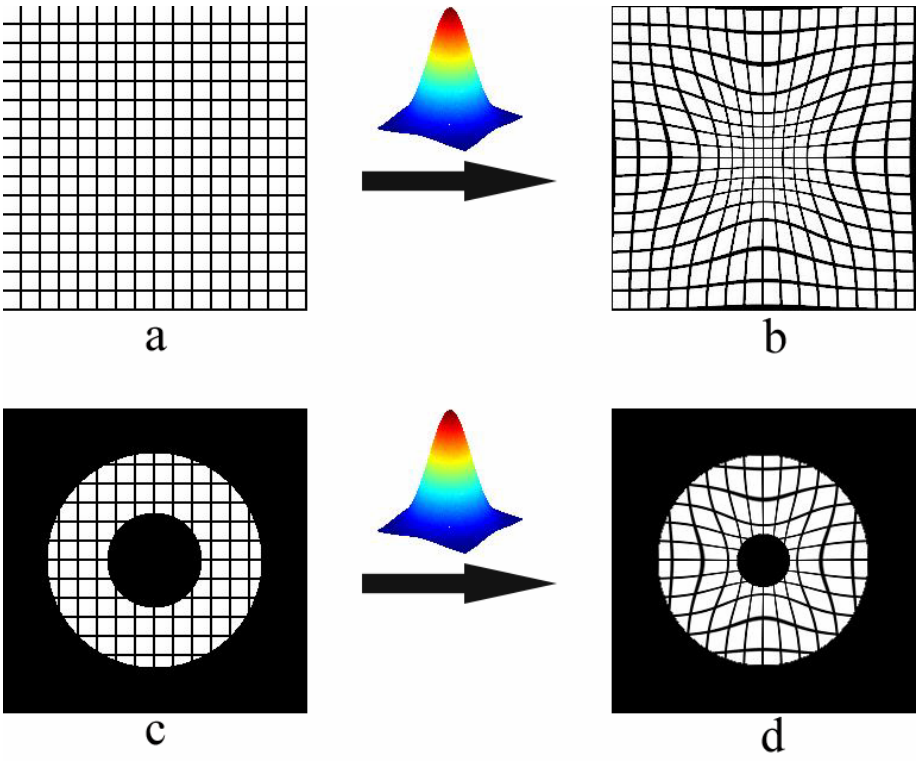

Figure 3.2

Algorithm describing the segmentation of the LV from a larger tagged image.

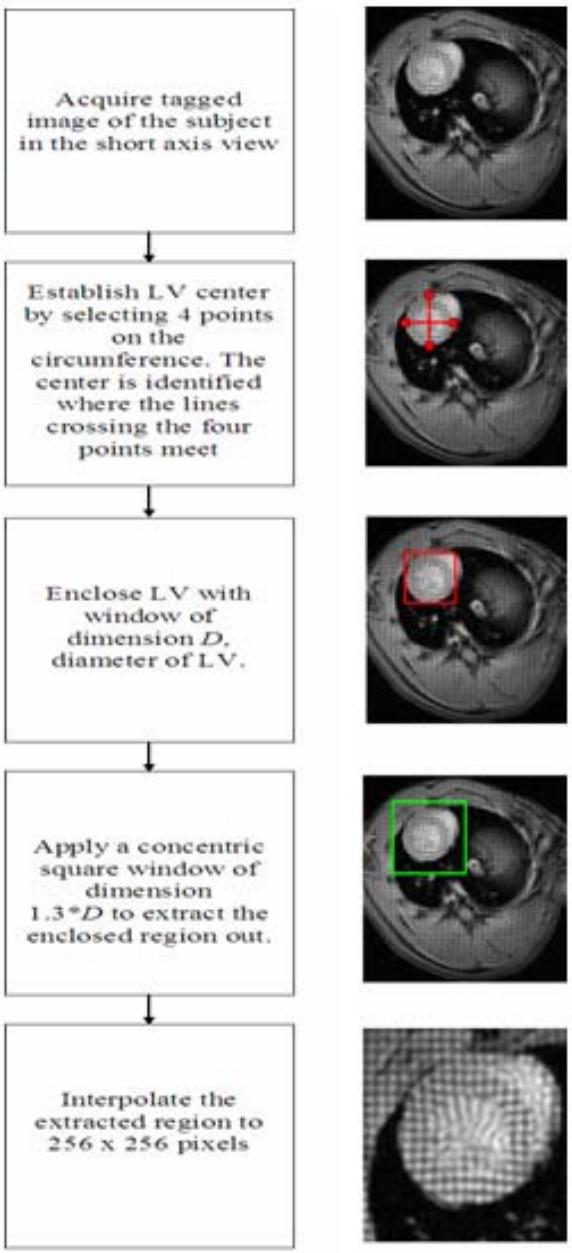

Figure 3.3

Segmented serial images (1-5) of the LV resized to 256x256 pixels during systole.

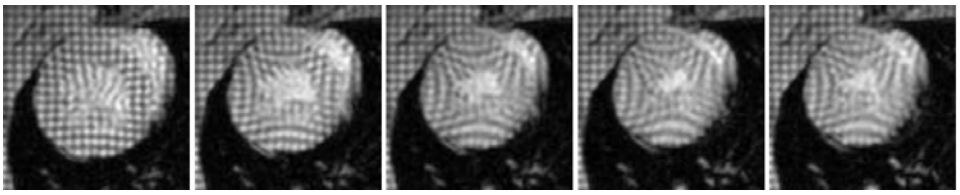

Figure 3.4

An algorithm to estimate an optimal value for the parameter α in the Gaussian transformation **T** using an image acquired at a systolic phase.

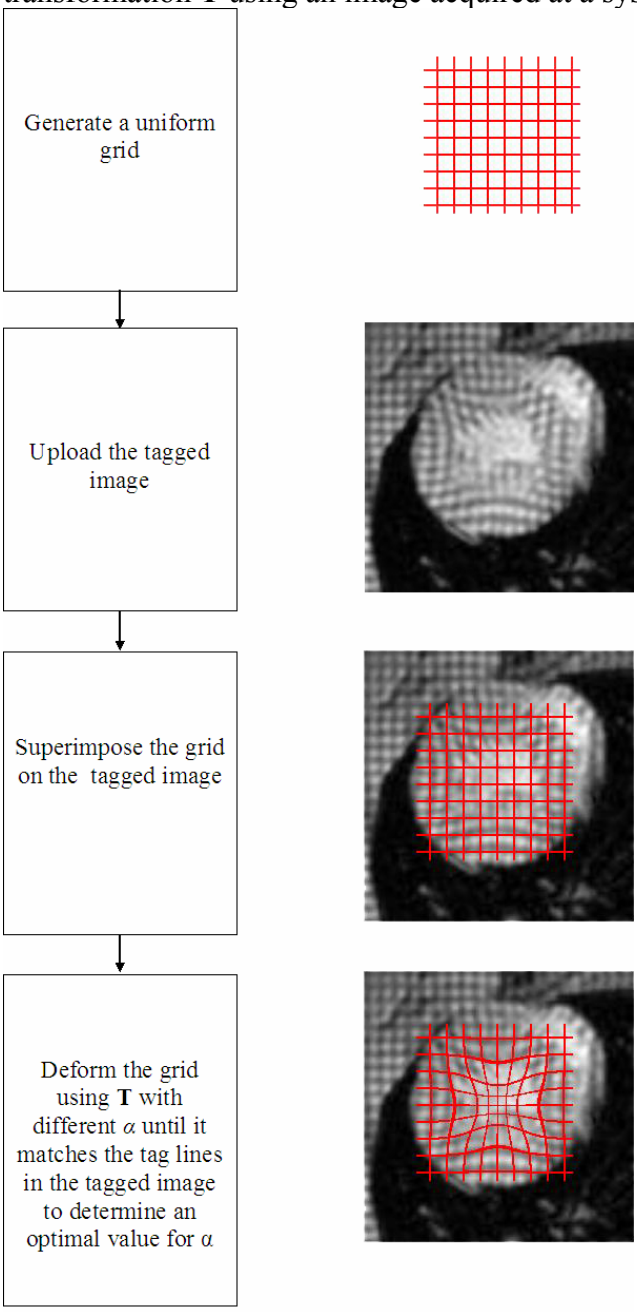

Figure 3.5

Real time systolic images (2-5) of the LV from Fig. 3. Superimposed is a grid (red) that was deformed offline using the Gaussian transformation **T** applied on the image 1 according to the algorithm in Figure 4. The grid (red) mimics the deformed tag lines in the underlying myocardial tissue. The estimated optimal α values are respectively 12, 16, 19 and 20.

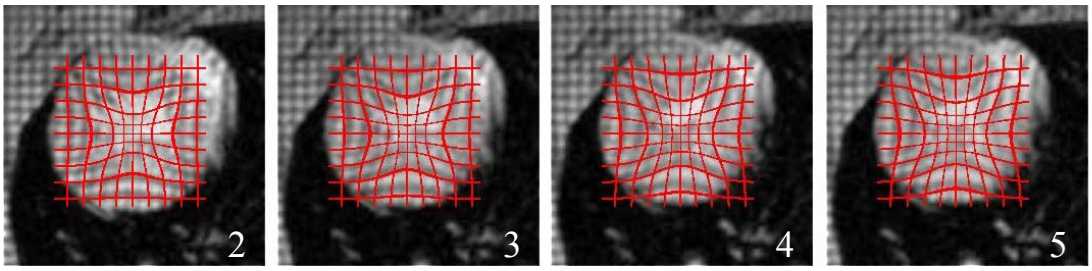

Figure 3.6

Real and simulated pseudo images in systole. The simulated images were obtained offline using the operation **T** on the real tagged image 1 with the optimal α values 12, 16, 19 and 20, as in Fig. 5.

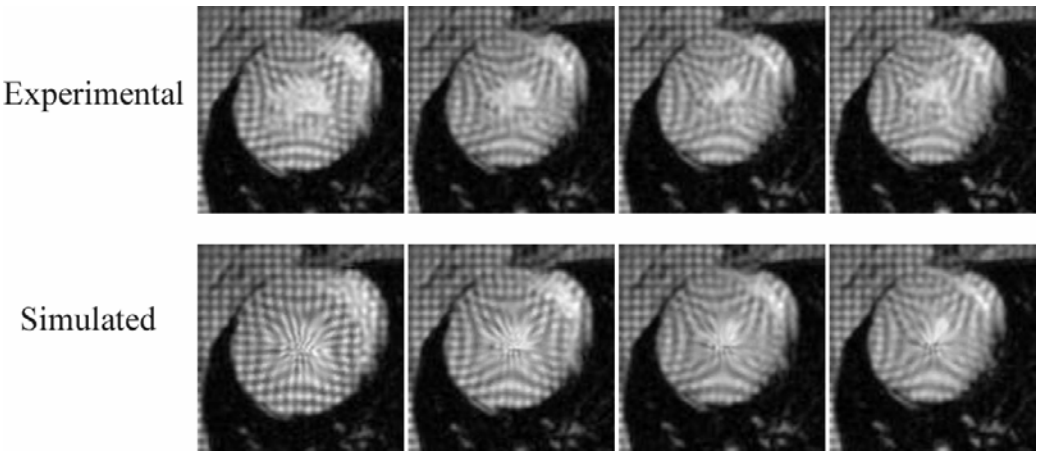

Figure 3.7

The deformation parameter α is plotted against the systolic image numbers, which are directly proportional to the acquisition time in the systolic phase. The curves in the graph show the results from the normal (n=4) and diabetic (n=1) rats.

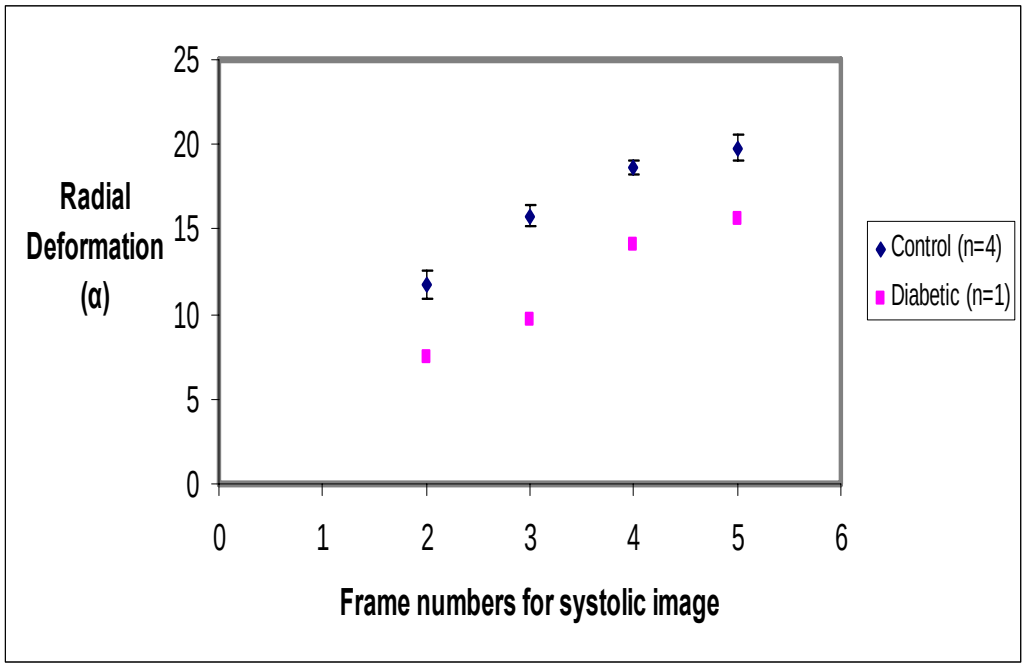

Table 3.1

The values (mean ± std) for the parameter α estimated using the data acquired from the control rats (n=4). Because the MR sequence applies tagging gradients in the image frame i=1(end diastole), the first noticeable deformation in tag lines occur s in frame i=2.

Frame	α (in pixels)
2	12.0 ± 0.8
3	16.0 ± 0.6
4	19.0 ± 0.4
5	20.0 ± 0.8

CHAPTER 4:
Part II
Time-reversal of radial motion to characterize regional deformation of the left ventricle using tagged MRI

This chapter consists of a manuscript submitted for peer review prior to publication.

It discusses a novel method to estimate motion of the left ventricle during systole.

Chapter Summary

Background: Myocardial motion is an important observable for assessment of heart condition. In Part I, we introduced a novel model to describe left ventricle (LV) wall motion in tagged magnetic resonance imaging (MRI) data using a Gaussian based transformation. In the current paper, we demonstrate the utility of the model in enhancing myocardial motion estimation through utilization of a time-reversal approach by inverting the Gaussian transformation.

Methods: Theoretical analysis leading to the construct of the time-reversal approach is discussed. A quantitative example is given to show the methodology of utilization of time-reversal approach using tagged MRI data. The utility of the approach is further demonstrated by incorporating it with harmonic phase (HARP) techniques.

Results: The time-reversal approach estimated the bulk portion of the motion of the myocardium from a subject population. The remaining residual portion of the motion was obtained from inter-variation calculations using HARP or similar techniques.

Conclusion: Utilizing a time-reversal approach enhances computation of the myocardial tissue motion. It can be utilized in combination with standard motion estimation techniques to yield improved estimates for the LV wall motion.

Introduction

In Part I, we introduced a simple forward model of the LV wall motion by utilizing a spatial operator based on a Gaussian transformation. This model mimics the motion of the myocardial tissue at the mid-ventricular level. In the model, a deformation parameter α was introduced to represent radial contractility of the LV, and accounts for the time variation of its shape and size in the systolic phase of the cardiac cycle. To standardize the cardiac motion with the model in a species-independent fashion, an offline image processing algorithm was designed to segment out the LV from the whole body tagged MRI data prior to the analysis of data. The extracted images with this preprocessing step included the LV alone and were expressed in pixel units. Using experimental data, the Gaussian transformation was characterized empirically to describe the forward systolic motion of the LV in normal rats. Fitting the LV model to the data obtained from a diabetic rat however yielded considerably different values for the parameter α. This observed difference demonstrated the model's capability and sensitivity to detect myocardial contractile deficiencies associated with a disease or a pathological condition that lead to a poor cardiac performance.

In this paper, another important utility of the Gaussian LV model is introduced in measuring the regional myocardial motion and quantifying the resulting deformation in the LV wall. Deformation is related to changes in relative distances between the myocardial tissues as they move during the cardiac cycle. Quantification of the deformation involves accurately measuring the motion and relative displacements

experienced by the myocardial tissue. To improve the performance of the myocardial motion estimation, this paper introduces a time-reversal concept where the forward LV model is applied on the real data, but in a reverse sense in time. The next section gives background information that led to the construction of the time-reversal operator, and describes details of the processing involved with an example. In Section 3, we demonstrate improvements in estimation of myocardial tissue displacement by using a motion tracking algorithm based-on harmonic phase (HARP) analysis [4, 6, 7]. We conclude the paper with a concise discussion and a recap in Section 4.

Time-reversal operation

Forward LV motion Model

The forward LV motion model at the mid-ventricle and its characterization were described in detail in Part I. The model is based on a Gaussian function encapsulated in an affine-like transformation operator, **T**, with diagonal elements that are identical to $1+e^{\frac{-(x^2+y^2)}{\alpha^2}}$. The parameters x and y in this expression represent spatial coordinates, and α is a time-dependent parameter accounting for the temporal changes in the LV size in the short-axis view at the mid-ventricle level. The real tagged MRI data were preprocessed by the algorithm developed in Part I, to yield the images I_i for i=1,2…L depicting the LV motion sequentially from end-diastole i=1 to end-systole i=L in equally spaced time intervals. The function of the operator **T** is to

deform the image canvas I_1 by an amount defined by α. Figure 4.1 shows the application of this operator using a digitally simulated data set. A uniform image $D_1(x,y)$ labeled with regularly spaced grid tags in Fig. 4.1-a is transformed to a deformed image, $D_2(x,y) = \mathbf{T}[D_1(x,y)]$, in Fig. 4.1-b. The operation yields the deformed image in Fig. 4.1-b, where the shape and size of the tag cells depict regional motion. If a donut-shaped disk in Fig. 4.1-c is used to mimic the LV wall, Fig. 4.1–d shows the resulting radially contracted disk.

The characterization of the forward LV model from real data requires finding an α_i value such that the computationally-deformed end-diastole image I_1 of the LV matches the image I_i in the sequence. Optimal α_i values obtained with this procedure for normal rat hearts are listed in Table 4.1.

Motivation and application of the time-reversal operation

During a cardiac cycle, the LV wall experiences relatively large motion as seen in Figure 4.2, which shows the image frames acquired sequentially within the systolic phase of a cardiac cycle. Quantifying the regional tissue deformation and assessing the local myocardial function and viability require estimates of the myocardial tissue displacements. The displacement measurement becomes a challenging task to perform especially when the motion between the two images in the sequence is large. Also, the statistical errors made during the estimation process increase with the magnitude of the motion. Although, sophisticated signal processing approaches may improve the estimation performance by minimizing such errors, these methods also demand significantly increased computation time, as in the case of motion tracking

algorithms employing window-based search techniques. In addition, signal decorrelation between the image frames in the presence of large deformations may also cause more difficulties in estimation. A severe decorrelation between windowed signals subsequently contributes to a poor outcome for the performance of displacement estimation. In our previous work in elastography imaging, we introduced global and adaptive regional signal stretching methods to compensate for these degrading effects and to yield better performance in displacement estimation under large tissue motion [4, 6, 7, 24-26]. The stretching procedures employed earlier were, however, directionally linear and uniform. In ultrasonic elastography, we globally decompressed the post-compression acoustic wave field composed of the backscattered signal received by each element of the array transducer by the same stretch value equivalent to the applied strain on the sample. In the adaptive stretching approach, the post-compression signals localized to a region within the ultrasonic wave field were expanded or compressed to increase the signal similarity with the pre-compression signals. Here, we adapt similar strategies and introduce a time-reversal operation to improve performance in tracking the LV wall motion from tagged MRI data. This adaptation utilizes the same Gaussian function defined in Part I for the systolic forward LV motion. In the current application, however, the Gaussian function is utilized to stretch the cardiac signals back in a radial fashion to the initiation of systole. This effect is demonstrated in Figure 4.3, where a deformed grid is restored to its pre-deformed state (Fig. 4.3a), and a deformed tagged donut is brought back to its original undeformed shape (Fig. 4.3b) by means of the time-

reversal operation. In this application, the forward model is essentially operated in reverse. Hence, in real MRI data, the forward model determined for the image frame i on the average is operated in reverse, but on an individual image from a given set of sequential images. The result is a time-reversed pseudo image where the LV wall shape and size are expected to be close to those seen in the image in frame i=1, acquired at the beginning of the systole in the image set. Thus, in cause and event terminology, the time-reversal operation attempts to reverse a displacement event, by inverting its cause, namely the systolic contraction. Mathematically, the time reversal of motion can be obtained by the operator $\mathbf{T}^{-1}$, i.e., the matrix-inverse of the forward motion operator $\mathbf{T}$.

The true displacement $\mathbf{d}$ of myocardial tissue at a spatial location in the LV wall can be decomposed into two components:

$$\mathbf{d} = \mathbf{\Delta} + \mathbf{\delta} \quad . \tag{4.1}$$

Here $\mathbf{\Delta}$ denotes the bulk motion predicted by the time-reversal model and its elements along the x and y directions are given by $xe^{\frac{-(x^2+y^2)}{\alpha^2}}$ and $ye^{\frac{-(x^2+y^2)}{\alpha^2}}$ respectively (from Eq. 3.1 in Part I). The term $\mathbf{\delta}$ is the residual displacement that is not accounted for by the time-reversal operation and remains to be estimated using algorithms applied between the image I_1 and the time-reversed image. However, because the residual displacement is smaller in magnitude as compared to the true displacement, the estimation results in small estimates with smaller errors.

To describe the above procedure in a compact form, we devise the following algorithm:

1. Obtain time-reversed image by applying $\mathbf{T}^{-1}$ to the desired image frame I_i using α_i.
2. Calculate the amount of bulk motion $\boldsymbol{\Delta}$ between the time-reversed image TR=$\mathbf{T}^{-1}[I_i]$ and image frame I_i using simple matrix multiplication.
3. Estimate the amount of residual motion $\boldsymbol{\delta}$ between the time-reversed image TR=$\mathbf{T}^{-1}[I_i]$ and the first systolic frame I_1 using a method of preference for the motion estimation, e.g., Harmonic Phase Analysis (HARP) [4, 6, 7, 27].
4. Add $\boldsymbol{\delta}$ to $\boldsymbol{\Delta}$ to yield a value for the estimate of the true total displacement **d**.

Results

Figure 4.4 illustrates the time-reversal operation applied to a real MRI data set – two image frames I_1 (Fig. 4.4-a) and I_2 (Fig. 4.4-b) are taken from a cardiac image sequence obtained from a normal rat heart. By applying the operation TR=$\mathbf{T}^{-1}[I_2(x,y)]$, the time-reversed image of the frame i=2 is obtained and displayed as a third image (Fig. 4.4-c) in the figure. Comparing the intensity features between the first and third images indicates that the LV wall size and dimensions on the time-reversed image TR are nearly restored to those seen on the image I_1, and the tag lines are straightened. Figure 4.5 depicts the images in Fig. 4.4 side-by-side and illustrates a material coordinate in the LV wall moves with real forward and time-reversed motions. The figure also depicts vertical components of the displacement described by Eq. 4.1. The displacement of the tissue at the selected coordinates appears to be

much smaller in the (I_1, TR) pair than it is in the (I_1, I_2) pair making the former pair a simpler choice for motion calculations in terms of the noise considerations. Once the residual motion profile between the image pair (I_1,TR) is estimated, the result is added to the bulk motion quantity obtained from the time-reversal to reach the final estimate of the motion between the image pair (I_1,I_2). Hence, the bulk motion quantity $\mathbf{\Delta}$ which is resembles the average from the subject population, is added to the residual quantity $\boldsymbol{\delta}$ that represents sample-dependent inter-variation, to yield a final motion estimate.

Potential application of the time-reversal operation to aid the analysis of cardiac motion using HARP

In this section, we further demonstrate how reversing an event (displacement) by inverting its cause (systolic contraction) can play a beneficial role in improving the performance of the motion estimation using HARP analysis. Below, we give a brief description of HARP and its methodology in computing myocardial motion from the tagged MRI data. For a thorough discussion of HARP, the reader is invited to see Refs. [4, 6, 7, 27].

HARP makes use of the information embedded in the Fourier spectrum of the tagged MRI data for the purposes of quantifying the cardiac motion. The tag patterns give rise to spectral peaks, also known as harmonic peaks, in the spectrum. The peak corresponding to the fundamental frequency defined by the separation of the tagged lines is extracted by means of a band-pass filter. Two filters were designed to select the vertical or horizontal tag line. Essentially, the inverse Hilbert transform of the

filtered spectrum has two signal parts, namely magnitude H and phase φ. The resulting complex signal H can be written as $\mathrm{H} = He^{j\varphi}$. While the magnitude is not of importance in motion quantification, the phase is considered to be the basis of the HARP analysis. It has been shown that phase information is directly linked to the material coordinates of the myocardial tissue, and therefore used for tracking and quantifying its Lagrangian motion.

The HARP analysis requires two filtered complex images H_1 and H_2 from which the displacement to be estimated from the phase difference in between using the formula

$$\varphi_2 - \varphi_1 = \angle\left(\mathrm{H}_2\mathrm{H}_1^{*}\right) = \angle\left(H_1 H_2 e^{j(\varphi_2 - \varphi_1)}\right). \tag{4.2}$$

The computed phase difference $(\varphi_2 - \varphi_1)$ however, wraps within the interval $[-\pi,\pi]$, especially in the presence of large motion between the two image frames. This effect is demonstrated in Figure 4.6, where a vertical motion map is produced from image sets I_1 and I_2 in Fig. 4.4 using Eq. 4.2. The large motion between the frames produces phase wraps, making it inadequate to accurately describe the motion. While phase unwrapping offers a remedy [27, 28] to this issue, its complex and computationally time consuming implementation is often a drawback. However, a simplified approach with a quick outcome can be provided by the time-reversal operation. Incorporation of the time-reversal operation prior to the HARP analysis yields more reliable results by avoiding sources that lead to phase wrapping. Since the $\mathbf{\Delta}$ component of a large motion **d** between two images is primarily responsible for the resulting phase wraps, its removal with the time-reversal operation leaves the

smaller magnitude component **δ** behind to be estimated using the HARP analysis. With this small **δ**, HARP analysis applied between the images I_1 and TR is expected to produce a motion map free of phase wraps. Figure 4.7 provides an example of such cooperation using both time-reversal and HARP methods, and shows that the phase wrapping is no longer an issue in the vertical motion map.

Conclusion

This paper presented a method to enhance the estimation performance of the regional myocardial motion measured from sequentially-acquired tagged MRI data. The method combines the Gaussian model of the real forward motion model of the LV wall, introduced in Part I, with the time-reversal operation to account for the large displacements experienced by the myocardial tissue. The remaining smaller deviations from the real motion can be estimated by an estimation technique of preference selected by the user. Following such a two-step approach reduces the computation time and errors made in the displacement measurements. If HARP is utilized for the analysis of the motion, the simple prior time-reversal operation applied on the data reduces the phase wrapping greatly and increases the accuracy of the displacement measurements while reducing the computational time. Motion estimates with reduced errors allows better interpretation of the results and enable computation of accurate strain fields to characterize the regional deformation aimed at evaluating the function, viability and pathological state of the underlying myocardial tissue.

Table 4.1

The values (mean ± std) for the parameter α estimated using the data acquired from the control rats (n=4). Because the MR sequence applies tagging gradients in the image frame i=1(end diastole), the first noticeable deformation in tag lines occur s in frame i=2.

Frame	α (pixels)
2	12.0 ± 0.8
3	16.0 ± 0.6
4	19.0 ± 0.4
5	20.0 ± 0.8

Figure Captions

Figure 4.1. A uniform image $I(x,y)$ in Fig. 1-a is labeled with regular grid tags. The operation $T[I(x,y)]$ yields the deformed image in Fig. 1-b, where the shape and size of the tag cells depict regional variations in motion. Similarly, a donut-shaped disk in Fig. 1-c is used as a simple model of the LV. Fig. 1–d shows the resulting deformed disk.

Figure 4.2. Systolic part of the cardiac cycle exhibits relatively large displacements due to large magnitudes of the myocardial motion.

Figure 4.3. Applying the operation $T^{-1}[T[I(x,y)]]$ on the deformed grid brings it back to an undeformed state (Fig. 1-a).

Similarly, a deformed donut shaped disk is brought back to an undeformed state through application of time reversal (Fig. 1-b).

Figure 4.4. Cardiac systolic motion changes image I_1 (a) to I_2 (b) causing large wall motion. Applying time-reversal to I_2 yields a time reversed image (c) with LV wall tissues almost restored to its initial positions in I_1.

Figure 4.5. Utilizing time reversal, the bulk motion Δ between I_2 and *TR* is computed using simple matrix multiplication. The residual motion δ between *TR* and I_1 is estimated by a method of preference, such as HARP.

Figure 4.6. The large magnitude of vertical motion between the two image frames gives rise to phase wraps in the HARP-based motion map (black arrows point at phase-wrapped regions). A mask is superimposed on the image frames to indicate the ROI.

Figure 4.7. Utilizing time-reversal computes motion between *TR* and I_2. Thus magnitude of motion is considerably reduced between *TR* and I_1 thereby yielding a phase-wrap free HARP motion map. A mask is superimposed on the image frames to indicate the ROI.

Figure 4.1

A uniform image $I(x,y)$ in Fig. 1-a is labeled with regular grid tags. The operation $\mathbf{T}[I(x,y)]$ yields the deformed image in Fig. 1-b, where the shape and size of the tag cells depict regional variations in motion. Similarly, a donut-shaped disk in Fig. 1-c is used as a simple model of the LV. Fig. 1–d shows the resulting deformed disk.

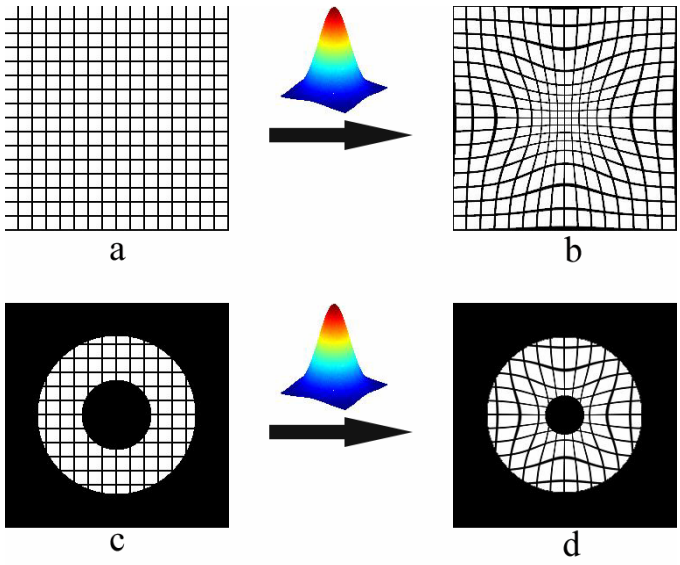

Figure 4.2

Systolic part of the cardiac cycle exhibits relatively large displacements due to large magnitudes of the myocardial motion.

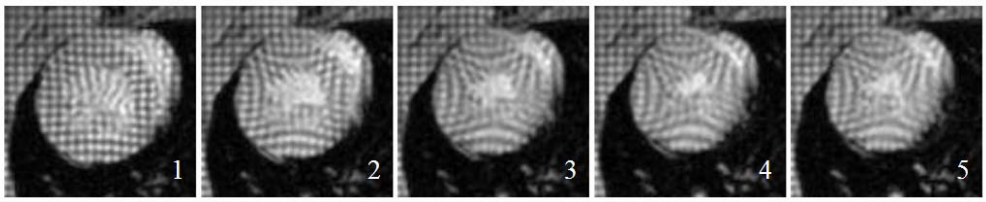

Figure 4.3

Applying the operation $\mathbf{T}^{-1}[\mathbf{T}[I(x,y)]]$ on the deformed grid brings it back to an undeformed state (Fig. 1-a).
Similarly, a deformed donut shaped disk is brought back to an undeformed state through application of time reversal (Fig. 1-b).

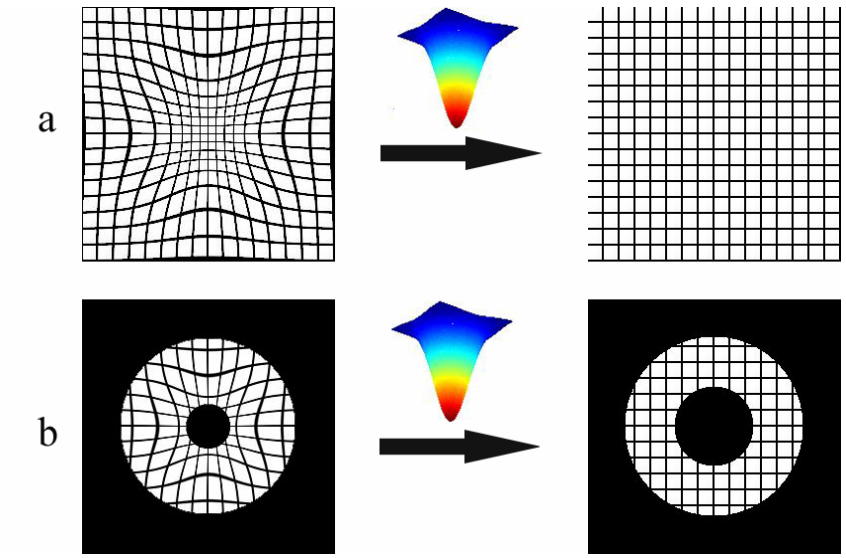

Figure 4.4

Cardiac systolic motion changes image I_1 (a) to I_2 (b) causing large wall motion. Applying time-reversal to I_2 yields a time reversed image (c) with LV wall tissues almost restored to its initial positions in I_1.

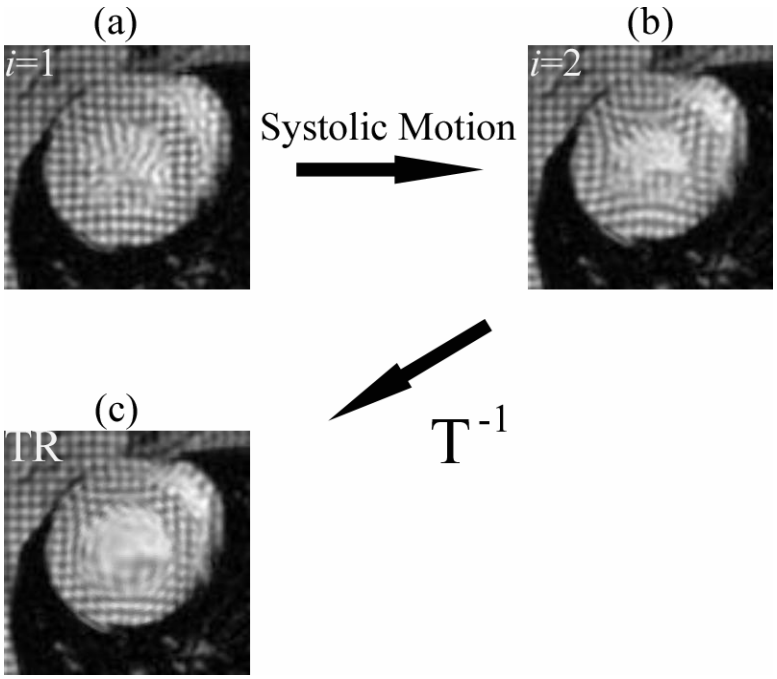

Figure 4.5

Utilizing time reversal, the bulk motion **Δ** between I_2 and *TR* is computed using simple matrix multiplication. The residual motion **δ** between *TR* and I_1 is estimated by a method of preference, such as HARP.

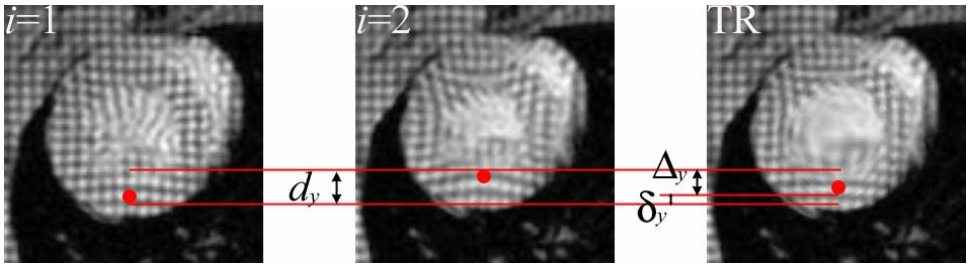

Figure 4.6

The large magnitude of vertical motion between the two image frames gives rise to phase wraps in the HARP-based motion map (black arrows point at phase-wrapped regions). A mask is superimposed on the image frames to indicate the ROI.

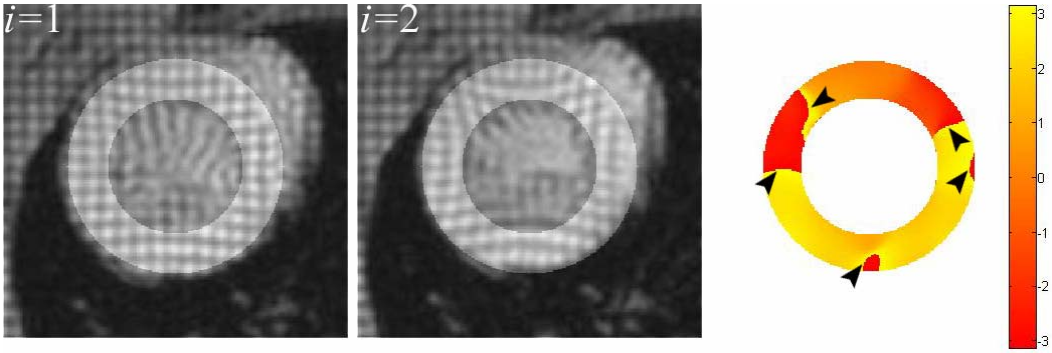

Figure 4.7

Utilizing time-reversal computes motion between *TR* and I_2. Thus magnitude of motion is considerably reduced between *TR* and I_1 thereby yielding a phase-wrap free HARP motion map. A mask is superimposed on the image frames to indicate the ROI.

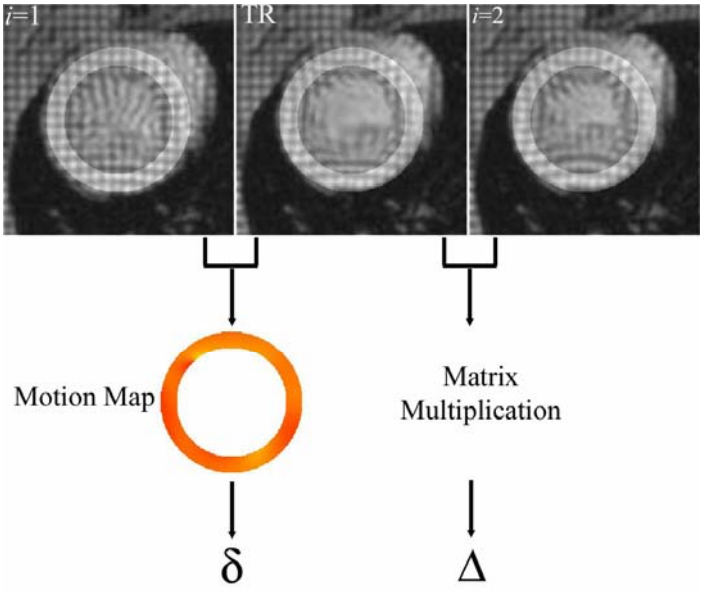

CHAPTER 5: SPIN-SPIN RELAXATION WITH RESPECT TO CARDIAC PHASE

Introduction

Spin-spin relaxation is the time required for the transverse magnetization M_{xy} to decrease by a factor of *e,* or loose 63% of its maximum value $M_{xy0,}$ following a 90° RF pulse. This relaxation time which is denoted by T2, is mainly due to loss of coherence between individual spins as a result of field inhomogeneities internal to the spin system. Such process does not involve loss of energy from the spin system; rather energy is exchanged between individual spins within the system allowing for dephasing and thus decay of M_{xy}. Transverse magnetization decay is governed by the transverse part of the Bloch equation in the rotating reference frame:

$$\frac{dM_{xy}}{dt} = \frac{-M_{xy}}{T2} \tag{5.1}$$

The solution for Eq. 1 is an exponential decay with T2 as the time constant (Figure 5.1)

$$M_{xy} = M_{xy0} \cdot e^{\frac{-t}{T2}} \tag{5.2}$$

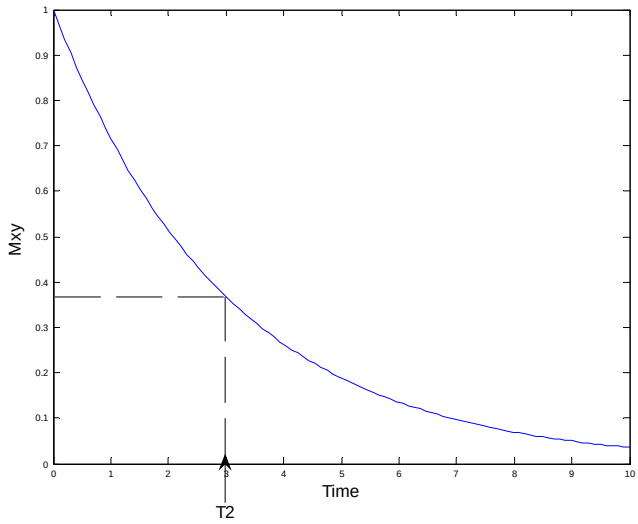

Figure 5.1:
Mxy decays exponentially.

Biological tissues are characterized by distinct T2 values. In general, T2 is prolonged for diseased tissues due to pathological processes of increasing water content associated with disease progression. This feature allowed measurement of T2 to play a key factor in identifying diseased regions [29-32]. .Measurement of T2 is typically performed with the widely used MRI spin-echo sequence [1] which is mathematically described as:

$$S = A(t) \cdot e^{\frac{-TE}{T2}} \qquad (5.3)$$

where S denotes the signal intensity, $A(t)$ is a time dependent sequence parameter, and TE is the echo time; a user controlled parameter to set the time between application of RF pulse and acquiring signal (Figure 5.2).

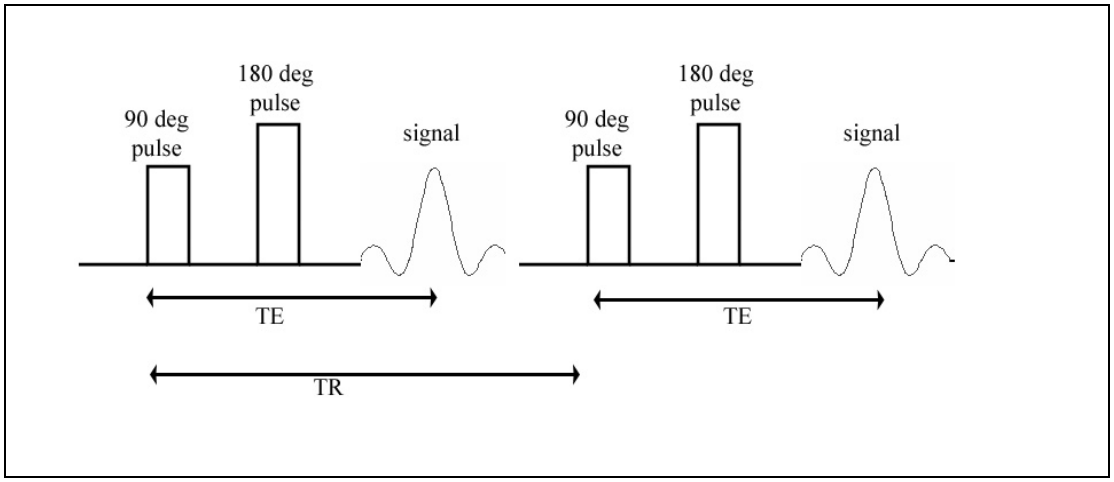

Figure 5.2: Spin-echo sequence with a 90 degree RF pulse. The echo time (TE) is the time between application of RF pulse and acquiring signal.

The typical spin-echo method of T2 calculation is based on acquiring two images with different echo times (TE1 and TE2), yielding different signal intensities (S1 and S2 respectively) [1]. Thus, T2 is calculated by:

$$T2 = \frac{TE2 - TE1}{\ln\left(\frac{S1}{S2}\right)} \qquad (5.4)$$

Table 5.1 lists measured T2 values for various biological tissues [33].

Table 5.1
T2 relaxation times in human subjects

Tissue	T2 (ms)	
	1.5 T	4 T
Gray matter	77-90	63
White matter	62-80	50
Muscle	31	26
Fat	47	38
Bone marrow	47	42

Unlike most tissues which are imaged in a motionless state, live myocardial tissues are in continuous motion due to contraction and relaxation of a beating heart. To avoid motion artifacts caused by this beating activity, proper utilization of electrocardiogram (ECG) gating is a typical practice in cardiac MRI studies where data acquisition is set in accordance to the heart rhythm. In addition, usage of ECG gating aids in selection of a specific cardiac phase such as end systole, where the resulting image represents a snapshot of the heart at the specified phase. Interestingly, it was reported that MRI signals of the myocardial during systole (contraction) are significantly higher than signals obtained during diastole (relaxation) [34]. This result which implies similar variation between T2 values of systolic and diastolic phases, acted as a motivator to investigate T2 variations with respect to cardiac phase. Consequently, an innovative method was required to enable selection of desired cardiac phases in conjunction with measurement of T2. Hence, the aim of this study is to develop a novel method to measure myocardial spin-spin

relaxation (T2) at various cardiac phases. Development of such method would aid in MRI research of a beating heart in addition to clinical applications of cardiac exams.

The rest of the chapter is organized as follows. The method of phase-selective T2 measurement is discussed in the next section. Section 3 describes the MRI experimental procedures used in the study, as well as offline image analyses. Display of the results and discussion of the outcome are presented in section 4, along with a summary and a recap of the study.

Phase-selective T2 measurement

This section presents an innovative method to measure the spin-spin relaxation time (T2) for a particular cardiac phase. The method has two main parts, experimental and computational. The experimental part deals with imaging aspects and data acquisition, while the computational part deals with offline calculations to obtain numerical values for the relaxation time T2. The experimental procedure starts with identifying the ECG temporal location of the desired phase with respect to the R-peak in the cardiac cycle. For example, if the desired phase is end systole the temporal location is ~ 125 ms for a typical R-R interval of 250 ms for a rat's heart (Figure 5.3). Hence, data must be acquired at the specific temporal location of 125 ms to yield a snapshot image at the desired phase of end systole. From Eq. 5.3, it is easy to see that signal intensity of the resulting image is a function of TE. Thus, acquiring a set of images at specified cardiac phase with different TE values requires separate experimental runs. Consequently, each run yields an equation similar to Eq.

5.3. Nevertheless, to target a specific cardiac phase it follows that consistent data acquisition is to be performed by accordingly adjusting the delay time (TD) of the ECG gating, and the echo time (TE) of the spin-echo sequence for each experimental run (Figure 5.4). For example, to target the end systolic phase (temporal location 125 ms), a four-run set of data requires TD=115, 105, 95, and 85 ms and TE=10, 20, 30 and 40 ms respectively in each run. Thus, in each run TD+TE yield the temporal location of the desired phase. Therefore, a four-run set of data yields four nonlinear equations to be solved numerically:

$$S_i = A \cdot e^{\frac{-TE_i}{T2}} \qquad i = 1..4 \qquad (5.5)\,.$$

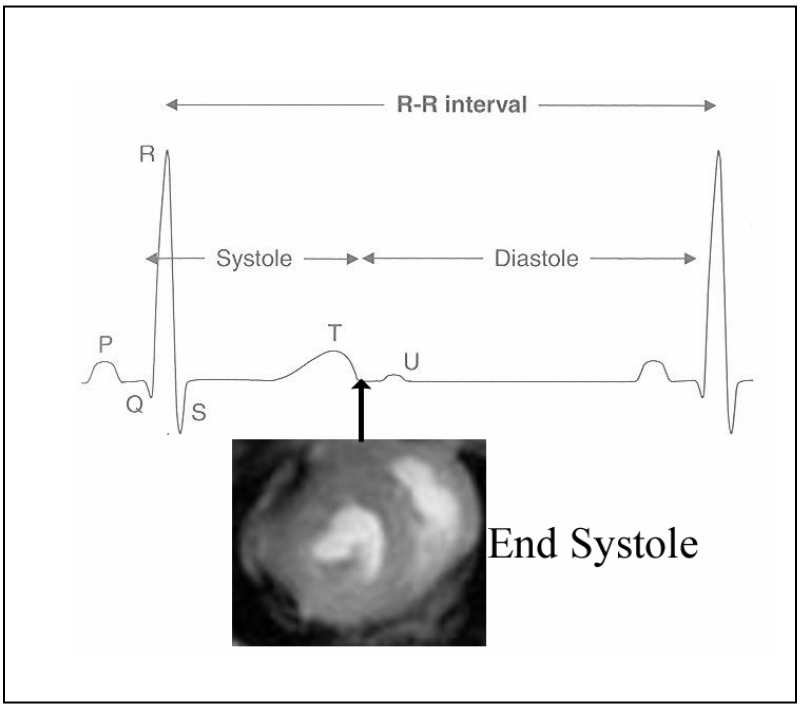

Figure 5.3: The figure shows temporal location of the end systolic phase with respect to the cardiac cycle.

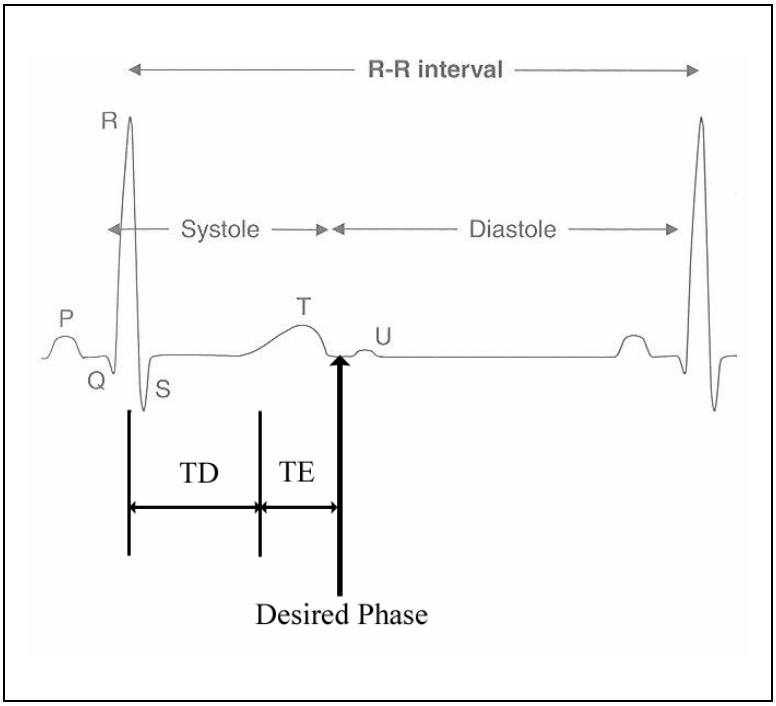

Figure 5.4: Selecting the desired cardiac phase requires TD+TE=const.

Exploiting the T2 exponential decay behavior, the computational part of the method utilizes a numerical scheme to solve sets of nonlinear four-equation systems [35, 36]. The scheme is mainly composed of a curve-fitting routine that implements least squares to find solutions for systems of equations. Thus, the routine finds the coefficient vector $\vec{c}$ that best fits the equation:

$$\frac{1}{2}\sum_{i=1}^{4}\left(F(\vec{c},TE_i)-S_i\right)^2 \qquad (5.6)$$

where $F(\vec{c},TE_i)=(c_1)\cdot e^{(c2)\cdot TE_i}$

The relaxation time T2 is equal to $\frac{1}{c_2}$, where $c_2 < 0$. Implementing the routine on a pixel by pixel basis yields a T2 map of the entire image, where each pixel carries a T2 value. Figures 5.5 and 5.6 show T2 maps obtained computationally from data acquired experimentally at end systole and end diastole phases respectively.

Methods and procedures

MRI Acquisition

Cardiac MRI data were collected at the mid-ventricle level from two normal Sprague-Dawley rats. The rats were anesthetized using 1.5 % isoflourane in a mixture of air and oxygen (60% and 40% respectively) and scanned using a 9.4 T horizontal bore scanner (Varian Inc., Palo Alto, CA) and 60 mm radio frequency volume coil. ECG gated cine-spin echo images were captured from the short axis view of the heart. For each rat , two sets of data were acquired; one at end systole and one at end diastole. Each data set consisted of four scan-runs where TD and the TE were varied for each run to target the desired cardiac phase as described above. Depending on the R-R interval period, TD and TE were slightly different for each animal. To target end systole, nominal values were TD=115, 105, 95, and 85 ms, and TE = 10, 20, 30, and 40 ms respectively. Similarly, to target end diastole, nominal values used where TD=230, 220, 210, and 200 ms and TE = 10, 20, 30, and 40 ms respectively. The following settings were used for image acquisition: repetition time (TR) = one cardiac cycle, number of averages = 1, field of view = 60 x 60 mm, image matrix = 256 x

256, slice thickness = 2 mm. All experimental procedures were approved by the University of Kansas Medical Center Institutional Animal Care and Use Committee.

Processing of MRI data

Raw MRI data was processed offline to obtain T2 maps of the LV region. All data sets from all rats were subject to the same processing operations. The process started by loading the four-run data set corresponding to a specific cardiac phase (end systole or end diastole) which were previously saved in fdf format to preserve pixel intensity values. Using the fdf images as input, a Matlab code with a least squares routine was implemented to fit a mono-exponential decay on a pixel by pixel basis yielding a T2 map of the entire axial slice covering the cross section of the animal. Next, a squared region containing the left ventricle (LV) was extracted from the T2 map and interpolated to 512 x 512 pixel-size yielding a T2 map consisting of the LV only. To select an ROI, unwanted regions such as the chamber and tissues surrounding the myocardium were masked out in the LV T2 map. Finally, an average T2 value was calculated for the selected ROI.

Results and discussion

In this study, the use of a phase selective data acquisition allowed for T2 measurement at specified cardiac phases, namely end systole and end diastole. Figure 5.5 shows a T2 map produced at end systole, along with associated MRI images acquired with different TE values. Similarly, Figure 5.6 shows T2 map along with

associated MRI images with different TE values captured at end diastole. Interestingly, calculating average T2 for the entire myocardial tissue yielded significantly higher T2 values for end systole than end diastole as listed in Table 2. This considerable difference in spin-spin relaxation is in accordance with the higher signal intensities observed at end systole as seen in Figure 5.7, where signal intensity is plotted against TE for both studied cardiac phases. Profiles of the curves in the figure agree with the theoretical exponential decay behavior of signal as a function of TE as described in Eq. 5.3. Moreover, fading of signal with higher TE is noticeable in Figs. 5.5 and 5.6, where some myocardial region exhibit dark pixel intensities.

The numerical scheme used to calculate T2 exploited the exponential decay behavior of signal with respect to TE. Such development helped in convergence of the curve-fitting routine, and hence in attainment numeric values for T2. Despite the small number of rats used in the study ($n = 2$), the statistical significance ($P < 0.02$) exhibited by the computed T2 values indicate the precision if the numerical scheme and its consistency with the experimental part. This successful integration between the constituents, namely experimental and numerical, led to the success of the phase-selective T2 measurement method as a whole.

In summary, this study investigated the relation of T2 with respect to cardiac phase for a beating heart. For quantitative analysis, a novel method was developed that allowed for T2 measurement for a specific cardiac phase. The method consisted of an experimental procedure to target a user-selected cardiac phase, as well as a numerical scheme to produce a T2 map of the entire myocardium. Although the

observed phases in this study were end systole and end diastole, the method is applicable for any phase in the cardiac cycle. To the best of our knowledge, this study is the first to present a method that allows for in vivo myocardial T2 measurement at a user-selected phase. The findings were in agreement with what was reported in the literature [34], thereby supporting the use of our method for in vivo cardiac investigations for phases of interest. Successful implementation of such method would promote its utility in cardiac MRI research as well as in clinical environments.

Table 5.2: Spin-spin relaxation for end systole and end diastole phases (mean ± std). Statistical significance was determined by $P<0.02$.

	T2 (ms)
End Systole	15.24 ± 0.92
End Diastole	11.04 ± 0.04

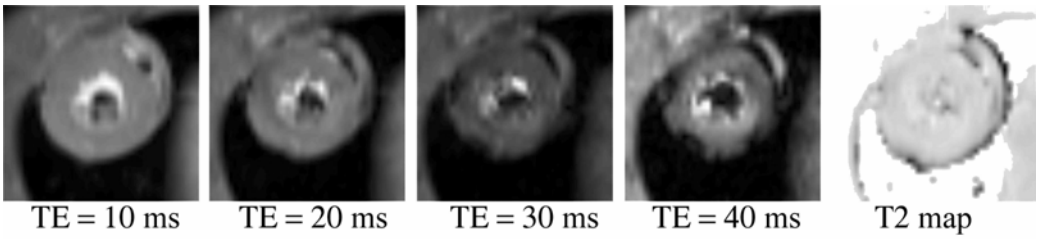

Figure 5.5:
Output of the phase selective method applied to end systole.

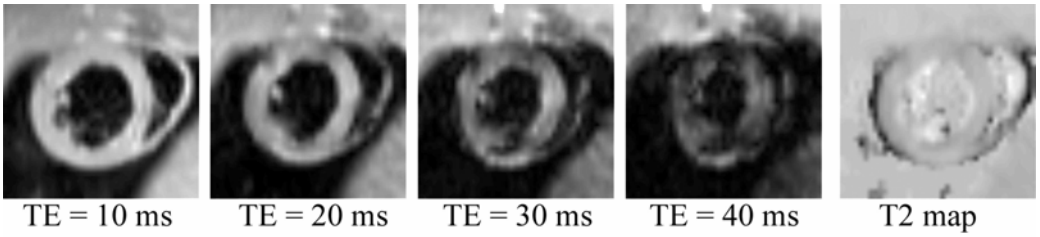

Figure 5.6:
Output of the phase selective method applied to end diastole.

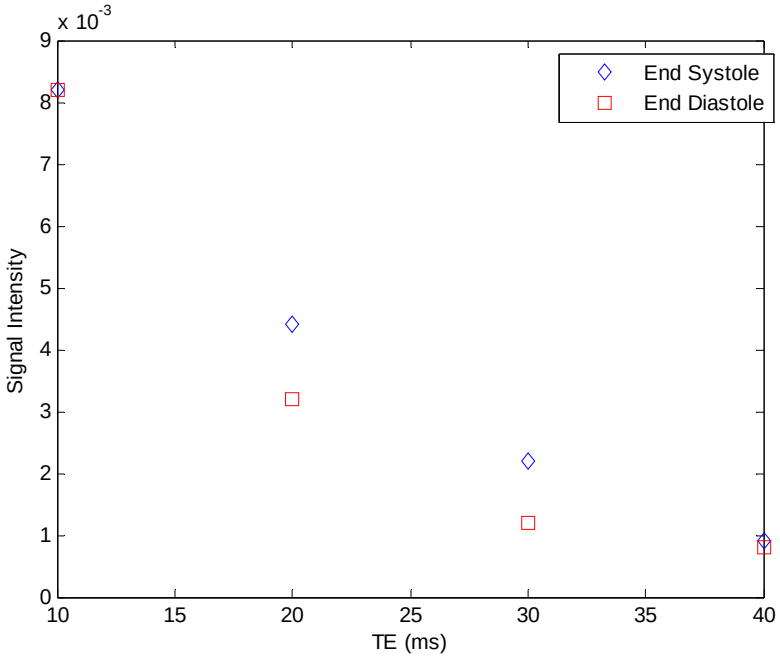

Figure 5.7:
Signal intensities fall with TE in an exponential decay. End systole exhibits higher signal than end diastole.

CHAPTER 6: IMAGE TRANSFORMATION TECHNIQUES

Introduction

The left ventricle (LV) goes through various modes of motion in a typical cardiac cycle [37-40]. Viewed from the short axis, LV tagged MRI images reveal myocardial deformation, elongation, shortening, and twist among other modes exhibited by LV wall tissue. While such motion is essential for pumping sufficient amounts of blood, its complexity poses a challenge for analyzing movement of myocardial tissue. Fortunately, image processing tools provide a remedy by de-synthesize complex motion through introducing a set of transformation operators. Hence, motion undergone by the LV disk is easily mimicked using digital perturbations that transform pixels to new locations according to defined mapping operations. Thus, the aim of this chapter is to present a set of transformation operators that are useful in mapping operations for digital images.

Synthetic data

The transformation operators presented in this chapter are applied on synthetic data for presentation purposes. This treatment was chosen to focus attention on motion-related effects without needing to account for noise and artifacts which often accompany real MRI data. Thus, the synthetic data used here are composed of a donut-shaped figure that resembles the LV disk in the short axis view. To imitate MRI tags, the figure is multiplied by a 2-D grid with user-controlled tag width and

separation. Hence, the resulting image reveals a tagged donut that depicts data obtained from tagged MRI procedures (Figure 6.1).

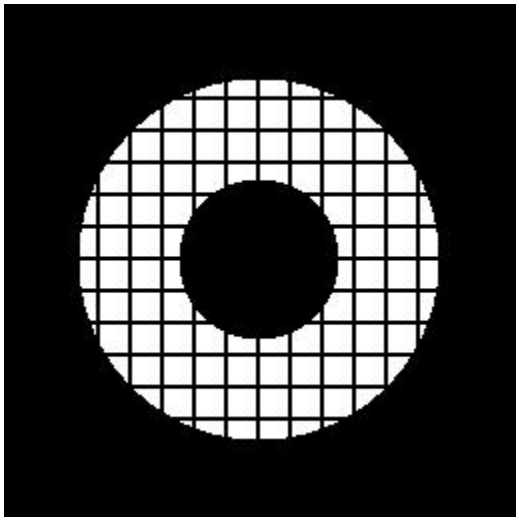

Figure 6.1:
Digital tagged donut represents LV image obtained in the short axis view from tagged MRI procedures.

Elongation and shortening

Among the simplest image transformations are elongation and shortening [41]. Mathematically, these two operations are generated by a diagonal matrix that is described as:

$$\begin{pmatrix} 1+\sigma_x & 0 \\ 0 & 1+\sigma_y \end{pmatrix}.$$

The parameters σ_x and σ_y produce changes in the *x* and *y* directions respectively. Positive values of either parameter result in elongation in the desired direction, while

negative values result in shortening. For $\sigma_x = \sigma_y = 0$, it is easy to see that the operator is reduced to the identity matrix. Figure 6.2 shows the effect of elongation and shortening on the tagged donut.

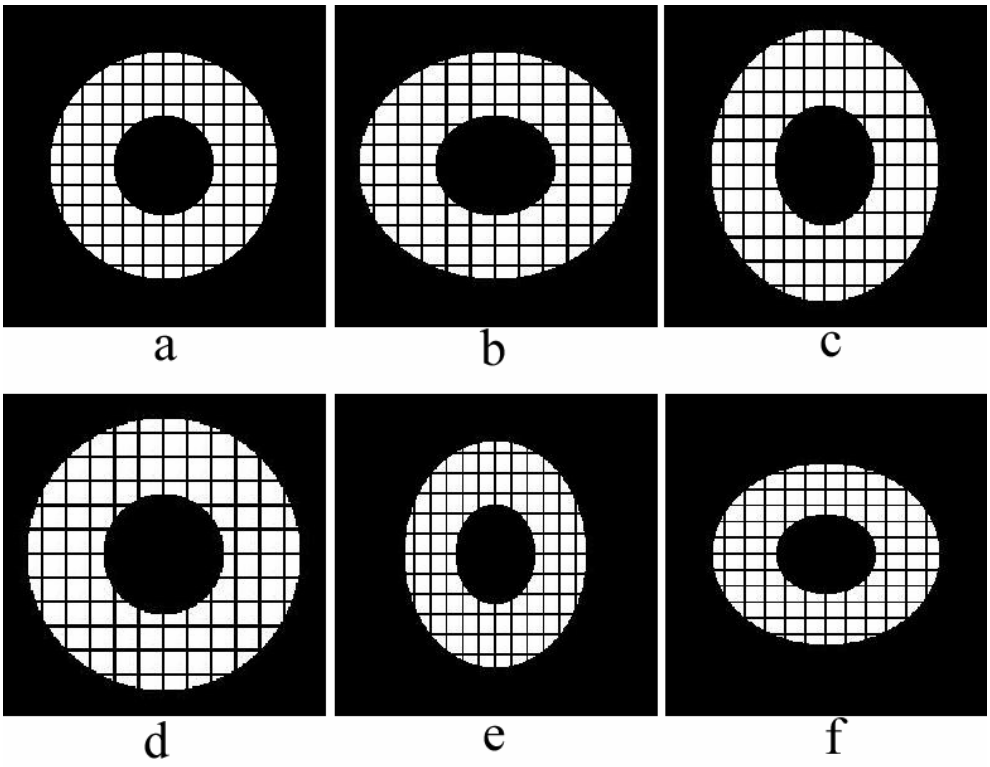

Figure 6.2
Tagged donut in (a) undergoes elongation of $\sigma_x = 0.2$ in (b), $\sigma_y = 0.2$ in (c) and $\sigma_x = \sigma_y = 0.2$ in (d). The donut undergoes shortening of $\sigma_x = -0.2$ in (e) and $\sigma_y = -0.2$ in (f).

Shear

Another simple transformation is shear [41]. The shear operator is described mathematically by:

$$\begin{pmatrix} 1 & \tau_x \\ \tau_y & 1 \end{pmatrix}.$$

The parameters τ_x and τ_y are responsible for shearing parallel to the x and y axes respectively. When both τ_x and τ_y vanish, it is easy to see that the operator reduces to the identity matrix. Figure 6.3 shows effect if the shear operator on the tagged donut.

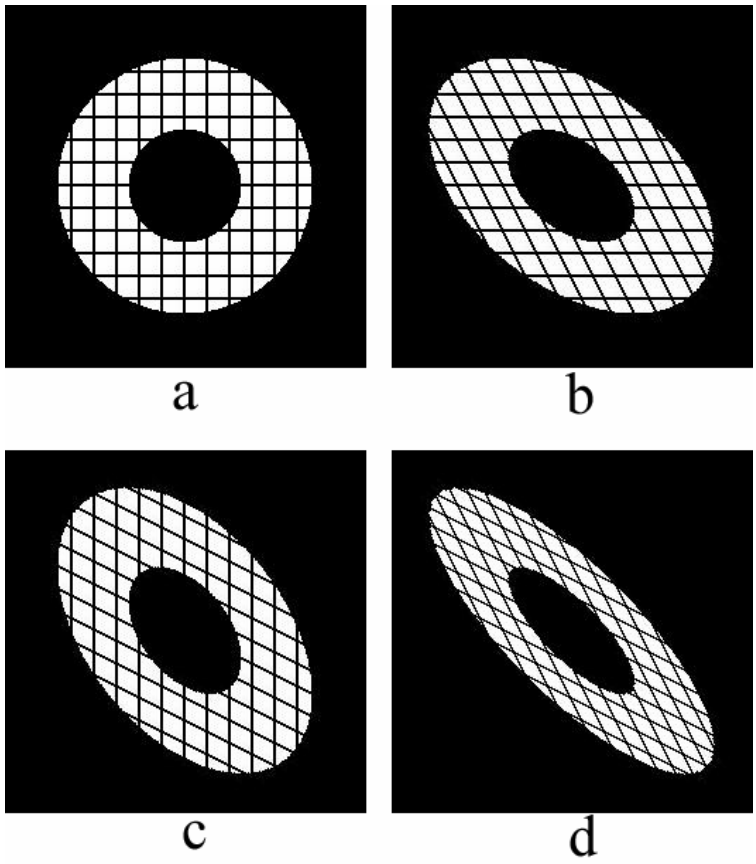

Figure 6.3
Tagged donut in (a) undergoes shear parallel to the *x* axis of $\tau_x = 0.5$ in (b), shear parallel to the *y* axis of $\tau_y = 0.5$ in (c) and shear parallel to both *x* and *y* axes of $\tau_x = \tau_y = 0.5$ in (d).

Rotation and twist

Rotation is considered among the basic and important image transformations [41]. Mathematically, rotating an image by an angle θ is achieved by applying the operator

$$\begin{pmatrix} \cos\theta & \sin\theta \\ -\sin\theta & \cos\theta \end{pmatrix}.$$

Positive values of θ yield counter clockwise rotation, while negative values yield clockwise rotation. Figure 6.4 shows effect of the rotation operator on the tagged donut.

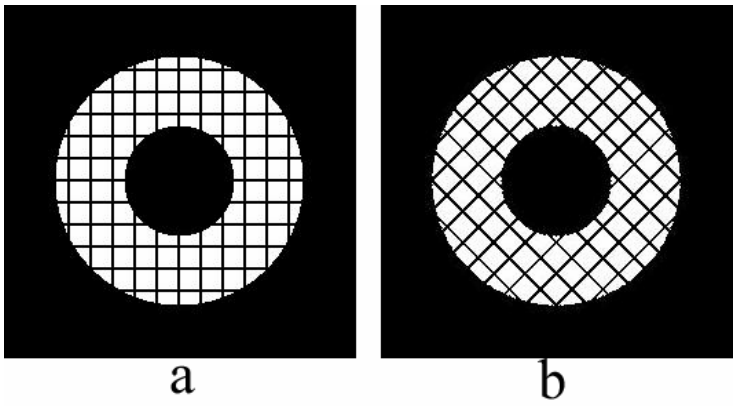

Figure 6.4
Tagged donut is rotated by 45 degrees.

The general case of rotation is twist, where the angle θ varies with location. For example, consider

$$\theta = m \cdot r^n \qquad (6.1)$$

where *m* and *n* are constants, and *r* is the distance from the center. Then, the rotation operator is used to apply twist on an image. Figure 6.5 shows the effect of twist in the tagged donut.

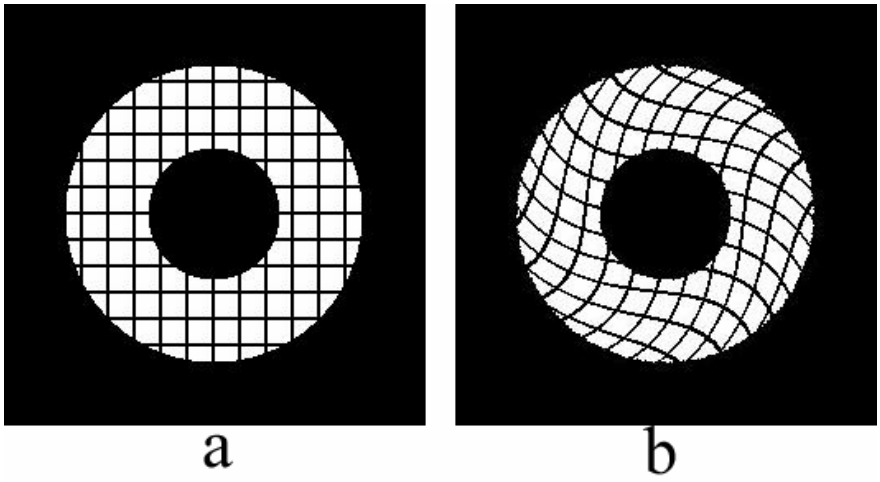

Figure 6.5
Tagged donut is twisted using values of 5E-5 and 2 for *m* and *n* respectively.

Translation

Another simple image transformation is translation [41]. Despite its simplicity, it differs from most operators by two main features. First, the translation operator is a vector, while most operators are square matrices. Second, the translation operator is added to the vector of the pixel to be translated, while most operators act through multiplication, not addition. Mathematically, the translation operator is described as

$$\begin{pmatrix} X \\ Y \end{pmatrix}.$$

The terms X and Y control translation along the x and y axes respectively. Figure 6.6 shows the effect of the translation operator on the tagged donut.

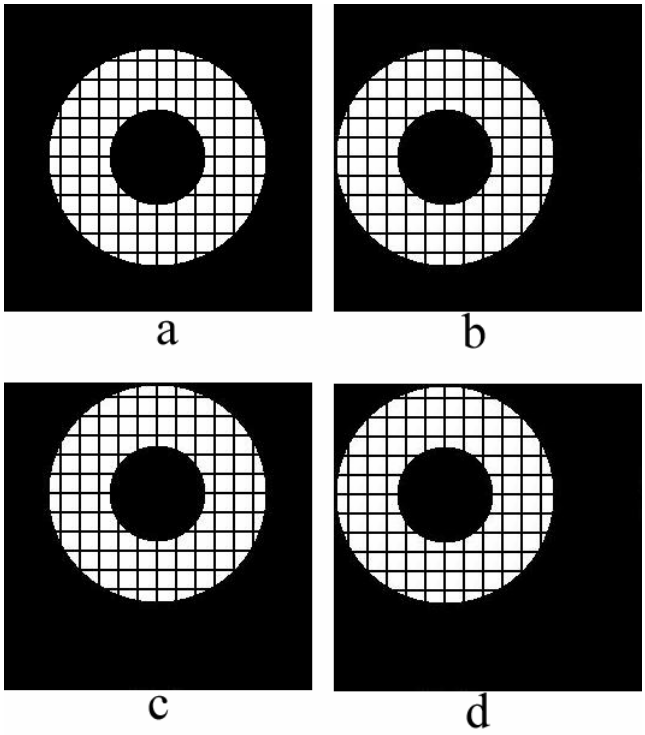

Figure 6.6
Tagged donut in (a) undergoes translation in the x direction by -35 (b), in y direction by 35 (c), in both directions simultaneously (-35 in x and 35 in y) (d).

ROI Tracking

The preceding discussion introduced image transformations in which pixels are relocated according to defined operations. The operators act as mapping functions where input and output images reveal differences in content position and geometry. The degree of difference depends mainly upon the magnitude and type of change set by the operators. Monitoring these changes is important for quantification purposes such as strain and displacement calculations. Yet, this monitoring activity requires ability to track user-selected regions of interest (ROI) throughout the duration of motion. Hence, this section presents a computerized procedure to track ROI in sequential image frames. The procedure is coded into interactive software that enables the user to select an ROI and track it through all image frames thereby monitoring motion and quantifying its evolution.

The tracking software presented herein was specially designed for images with tagging grids that are similar to tagged MRI data. The software utilizes tagging patterns as borders that define individual regions, where each region is a traceable ROI. Upon execution, the user is prompted to select an ROI in the first image frame. Next, the software converts the image to binary form and identifies the ROI using connectivity features of binary images. The ROI is simply identified as a connected body of 1's surrounded by a ring of 0's. Then the centroid of the ROI is calculated and the binary form of the second image frame is uploaded. Under the small motion assumption, the location of the ROI centroid in the first frame should lie within the ROI in the second frame, and the ROI is thus tracked. Next, the centroid of the

tracked ROI of the second frame is calculated and the procedure is repeated with the third and subsequent frames. Figure 6.7 shows an ROI (in red) that was tracked through 6 consecutive frames.

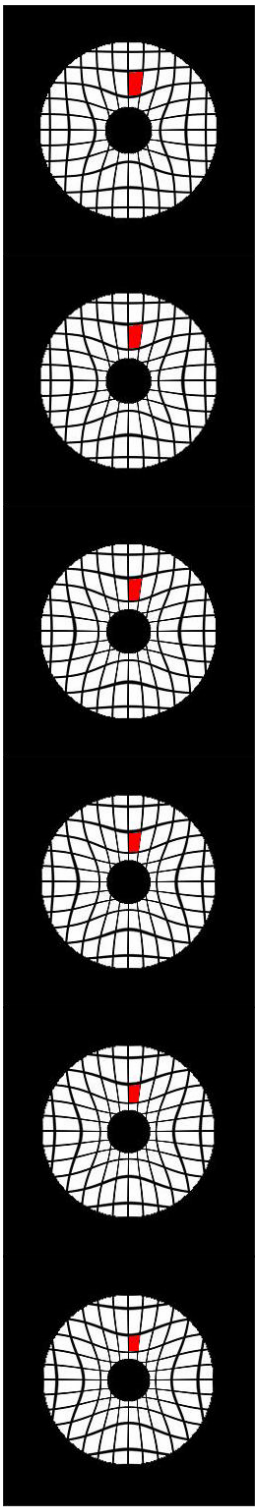

Figure 6.7
User-selected ROI (red) is tracked throughout the motion using the tracking procedure described in the text.

Conclusion

This chapter presented image transformations that mimic motion exhibited by the LV in the short axis view. The transformations were performed on digital data by virtue of mapping functions that relocated pixels to new positions according to user-defined operators. The mimicked motion included elongation, shortening, shear, rotation and twist. Moreover, the chapter introduced a novel tracking software that enables the user to track an ROI throughout all phases of motion. Thus, the transformation operators and the tracking software compose a computerized toolbox that aid in analyzing LV motion.

APPENDIX A

This appendix contains Matlab software of a graphical user interface (GUI) used to transform images [35, 41]. The GUI which is composed of one main program and seven subroutines, gives the user freedom to choose the type of transformation in addition to track regions of interest (ROI). Built with a user-friendly environment, the GUI utilizes image transformation operators discussed in chapter 6.

Main program

```
function image_deform(arg)
global H_popup    Hf_1  Hf_2
global  a

if nargin ==0
    arg='Initialize';
end
switch arg
    case 'Initialize'
        Hf_1 = figure ('Position' , [200 50 310 400]); % figure
(parent of all)  [200 50 1000 600]

H_browse_button = uicontrol(Hf_1 , 'Style' , 'pushbutton',
'Position', [10 150 150 25], 'String' , 'Browse Image');
set(H_browse_button, 'Callback' , 'image_deform Browse')




H_popup = uicontrol(Hf_1 , 'Style' , 'popup', 'String' , 'Stretch /
Shear|Rotation / Twist|Translation|Gaussian|Track' , 'Position' ,
[20 280 100 20] );
H_text_above_popup = uicontrol(Hf_1 , 'Style' , 'text' , 'Position'
, [10 299 90 20], 'String' , 'Deformation Type', 'BackgroundColor',
[0.8 0.8 0.8]) ; %
set(H_popup, 'Callback' , 'image_deform Popup')


logo=imread('logo.jpg');
        H_pic_button = uicontrol(Hf_1 , 'Style' , 'pushbutton',
'Position', [220 55 83 53], 'cdata' ,logo );

case 'Browse'
```

```
    [filename , pathname]=uigetfile({'*.jpg','JPEG (*.jpg)'},'Open
File');
    file_string=strcat(pathname,filename);
    a=imread(file_string,'jpg');
    figure , imshow(a);

    case 'Popup'
         p = (get(H_popup , 'Value'));
         if p==1 % Affine option
%
image_stretch % function image affine

     elseif p==2
         image_rotate
    elseif p==3
         image_translate
   elseif p==4
         image_gaussian
%    elseif p==5
%          image_stack
  elseif p==5
         image_track
 end % end if
end % end function
```

Stretch and shear subroutine

```
function image_stretch(arg)
global Hf_2 Hf_2_edit_box_stretch_in_x Hf_2_edit_box_stretch_in_y
Hf_2_edit_box_shear_in_x Hf_2_edit_box_shear_in_y Hf_2_save_button
%AI_G
global a
if nargin ==0
    arg='Initialize';
end
switch arg
     case 'Initialize'
Hf_2 = figure ('Position' , [300 90 400 400]);

Hf_2_edit_box_stretch_in_x = uicontrol(Hf_2 , 'Style' , 'edit',
'Position' , [20 360 130 20]); %


Hf_2_text_above_stretch_in_x = uicontrol(Hf_2 , 'Style' , 'text',
'Position' , [20 380 130 20], 'String' , 'Stretch in y',
'BackgroundColor', [0.8 0.8 0.8]) ; % string, written above edit box
```

```
Hf_2_edit_box_stretch_in_y = uicontrol(Hf_2 , 'Style' , 'edit',
'Position' , [160 360 130 20]); %


Hf_2_text_above_stretch_in_y = uicontrol(Hf_2 , 'Style' , 'text',
'Position' , [160 380 130 20], 'String' , 'Stretch in x',
'BackgroundColor', [0.8 0.8 0.8]) ; % string, written above edit box

Hf_2_edit_box_shear_in_x = uicontrol(Hf_2 , 'Style' , 'edit',
'Position' , [20 260 130 20]); %


Hf_2_text_above_shear_in_x = uicontrol(Hf_2 , 'Style' , 'text',
'Position' , [20 280 130 20], 'String' , 'Shear in y',
'BackgroundColor', [0.8 0.8 0.8]) ; % string, written above edit box


Hf_2_text_above_shear_in_y = uicontrol(Hf_2 , 'Style' , 'text',
'Position' , [160 280 130 20], 'String' , 'Shear in x',
'BackgroundColor', [0.8 0.8 0.8]) ; % string, written above edit box

Hf_2_edit_box_shear_in_y = uicontrol(Hf_2 , 'Style' , 'edit',
'Position' , [160 260 130 20]); %



Hf_2_deform_button = uicontrol(Hf_2 , 'Style' , 'pushbutton',
'Position', [20 60 130 20], 'String' , 'Deform');
set(Hf_2_deform_button, 'Callback' , 'image_stretch Deform')

% Hf_2_save_button = uicontrol(Hf_2 , 'Style' , 'pushbutton',
'Position', [170 60 130 20], 'String' , 'Save');
%  set(Hf_2_save_button, 'Callback' , 'image_stretch Save')

case 'Deform'
     X = str2double(get(Hf_2_edit_box_stretch_in_x, 'String'));
     Y = str2double(get(Hf_2_edit_box_stretch_in_y, 'String'));
     S_X=str2double(get(Hf_2_edit_box_shear_in_x,'String'));
     S_Y =str2double(get(Hf_2_edit_box_shear_in_y,'String'));
     c=128;
     w=waitbar(0,'Please Wait ...');
    for x_d=1:256
        waitbar(x_d/256);
    for y_d=1:256

        O = [X S_X; S_Y Y];
        A_S= inv(O) * ( [x_d;y_d]-[c;c])+[c;c];

        x_s=round(A_S(1));
        y_s=round(A_S(2));
        if x_s > 256 || x_s <=0
```

```
            x_s=1;
        end
        if y_s > 256 || y_s <=0
            y_s=1;
        end

        AI_G(x_d,y_d)=a(x_s,y_s);

    end
    end
close (w)
   figure , imshow(AI_G)
%    imwrite(AI_G,'new_sheared_image.jpg','jpg')
%     case 'Save'
%         imwrite(AI_G,'new_stretched_image.jpg','jpg')
end % end function
```

Rotation and twist subroutine

```
function image_rotate(arg)
global Hf_3 Hf_3_radio_button_rotation Hf_3_radio_button_twist
Hf_3_deform_button p q Hf_3_edit_box_rotation Hf_3_edit_box_twist_m
Hf_3_edit_box_twist_n
global a
if nargin ==0
    arg='Initialize';
end

switch arg
     case 'Initialize'
Hf_3 = figure ('Position' , [300 90 400 400]);

Hf_3_radio_button_rotation = uicontrol(Hf_3,'Style' ,
'RadioButton','Position',[20 360 130 20], 'String','Rotation',
'BackgroundColor', [0.8 0.8 0.8]);
set(Hf_3_radio_button_rotation, 'Callback', 'image_rotate
rotation_button')


Hf_3_radio_button_twist=uicontrol(Hf_3,'Style' ,
'RadioButton','Position',[20 230 130 20], 'String','Twist',
'BackgroundColor', [0.8 0.8 0.8]);
set(Hf_3_radio_button_twist, 'Callback', 'image_rotate
twist_button')

Hf_3_edit_box_twist_m = uicontrol(Hf_3, 'Style' , 'edit',
'Position',[20 180 130 20]);
Hf_3_text_above_twist_m = uicontrol(Hf_3, 'Style', 'text',
'Position',[20 200 130 20], 'String' , 'm', 'BackgroundColor',[0.8
0.8 0.8]);
```

```
Hf_3_edit_box_twist_n = uicontrol(Hf_3, 'Style' , 'edit',
'Position',[180 180 130 20]);
Hf_3_text_above_twist_n = uicontrol(Hf_3, 'Style', 'text',
'Position',[180 200 130 20], 'String' , 'n', 'BackgroundColor',[0.8
0.8 0.8]);


Hf_3_deform_button = uicontrol(Hf_3 , 'Style' , 'pushbutton',
'Position', [20 60 130 20], 'String' , 'Deform');
 set(Hf_3_deform_button, 'Callback' , 'image_rotate Deform')

 Hf_3_edit_box_rotation = uicontrol(Hf_3 , 'Style' , 'edit',
'Position' , [20 310 130 20]); %


Hf_3_text_above_rotation = uicontrol(Hf_3 , 'Style' , 'text',
'Position' , [20 330 130 20], 'String' , 'Constant Angle',
'BackgroundColor', [0.8 0.8 0.8]) ; % string, written above edit box


text(0.4,1.05,'\bf\theta = const.', 'FontSize', 18)
text(0.4, 0.6, '\bf\theta = m \times r^{n}', 'FontSize', 18)
axis('square')
axis off

% if one button is on, the other must be off
    case 'rotation_button'
        p = (get(Hf_3_radio_button_rotation , 'Value'));
        q = (get(Hf_3_radio_button_twist , 'Value'));

    set(Hf_3_radio_button_twist, 'Value', 0)



case 'twist_button'
        p = (get(Hf_3_radio_button_rotation , 'Value'));
        q = (get(Hf_3_radio_button_twist , 'Value'));

    set(Hf_3_radio_button_rotation, 'Value', 0)




case 'Deform'
if p==1 %rotation
    theta = str2double(get(Hf_3_edit_box_rotation, 'String'));
    theta=theta * pi/180;
    c=128;
     w=waitbar(0,'Please Wait ...');
```

```
    for x_d=1:256
        waitbar(x_d/256);
    for y_d=1:256

        O = [cos(theta) sin(theta); -sin(theta) cos(theta)];
        A_S= inv(O) * ( [x_d;y_d]-[c;c])+[c;c];

        x_s=round(A_S(1));
        y_s=round(A_S(2));
        if x_s > 256 || x_s <=0
            x_s=1;
        end
        if y_s > 256 || y_s <=0
            y_s=1;
        end

        AI_G(x_d,y_d)=a(x_s,y_s);

    end
    end
close (w)
   figure , imshow(AI_G)

elseif q==1

    m = str2double(get(Hf_3_edit_box_twist_m, 'String'));
    n = str2double(get(Hf_3_edit_box_twist_n, 'String'));
        c=128;
     w=waitbar(0,'Please Wait ...');
    for x_d=1:256
        waitbar(x_d/256);
    for y_d=1:256
        r=sqrt((x_d - 128)^2 + (y_d-128)^2);
        theta = m * r^n;
        O = [cos(theta) sin(theta); -sin(theta) cos(theta)];
        A_S= inv(O) * ( [x_d;y_d]-[c;c])+[c;c];

        x_s=round(A_S(1));
        y_s=round(A_S(2));
        if x_s > 256 || x_s <=0
            x_s=1;
        end
        if y_s > 256 || y_s <=0
            y_s=1;
        end

        AI_G(x_d,y_d)=a(x_s,y_s);

    end
    end
close (w)
   figure , imshow(AI_G)
```

```
end % end if rotation
     %imwrite(AI_G,'new_rotate_image.jpg','jpg')
end % end function
```

Translation subroutine

```
function image_translate(arg)
global Hf_4  Hf_4_edit_box_trans_x Hf_4_edit_box_trans_y
Hf_4_deform_button  Hf_4_save_button   AI_G
global a
a=im2double(a);
if nargin ==0
    arg='Initialize';
end
switch arg
     case 'Initialize'
Hf_4 = figure ('Position' , [300 90 400 400]);

Hf_4_edit_box_trans_x = uicontrol(Hf_4, 'Style' , 'edit',
'Position',[20 180 130 20]);
Hf_4_text_above_trans_x = uicontrol(Hf_4, 'Style', 'text',
'Position',[20 200 130 20], 'String' , 'Translation in y',
'BackgroundColor',[0.8 0.8 0.8]);

Hf_4_edit_box_trans_y = uicontrol(Hf_4, 'Style' , 'edit',
'Position',[180 180 130 20]);
Hf_4_text_above_trans_y = uicontrol(Hf_4, 'Style', 'text',
'Position',[180 200 130 20], 'String' , 'Translation in x',
'BackgroundColor',[0.8 0.8 0.8]);

Hf_4_deform_button = uicontrol(Hf_4 , 'Style' , 'pushbutton',
'Position', [20 60 130 20], 'String' , 'Deform');
 set(Hf_4_deform_button, 'Callback' , 'image_translate Deform')

 Hf_4_save_button = uicontrol(Hf_4 , 'Style' , 'pushbutton',
'Position', [170 60 130 20], 'String' , 'Save');
 set(Hf_4_save_button, 'Callback' , 'image_translate Save')

 case 'Deform'

     X = str2double(get(Hf_4_edit_box_trans_x, 'String'));
     Y = str2double(get(Hf_4_edit_box_trans_y, 'String'));
      c=128;
     w=waitbar(0,'Please Wait ...');
 for x_d=1:256
        waitbar(x_d/256);
    for y_d=1:256
```

```
        O = [1 0; 0 1];
        A_S= inv(O) * ( [x_d;y_d]-[c;c])+[c;c] + [X;Y];

        x_s=round(A_S(1));
        y_s=round(A_S(2));
%         if x_s > 256 || x_s <=0 || y_s > 256 || y_s <=0
%             AI_G(x_d,y_d)=0
%         else
%             AI_G(x_d,y_d)=a(x_s,y_s);
%         end
        if x_s > 256 || x_s <=0
             x_s = x_s-256;
        end
        if y_s > 256 || y_s <=0
            y_s = y_s-256;
        end

        AI_G(x_d,y_d)=a(x_s,y_s);

    end
    end
close (w)
   figure , imshow(AI_G)

   case 'Save'

       imwrite(AI_G,'new_translated_image.jpg','jpg')
end % end func
```

Gaussian deformation subroutine

```
function image_gaussian(arg)
global Hf_5 Hf_5_deform_button Hf_5_edit_box AI_G aa
global a

a=im2double(a);
if nargin ==0
    arg='Initialize';
end
switch arg
     case 'Initialize'
Hf_5 = figure ('Position' , [300 90 400 400]);
text(0.4,1.05,'\bf 1 + e^{-r^{2}/\alpha^[10]}', 'FontSize', 18)
text(0.1, 0.55, '\bf\alpha^[10]', 'FontSize', 18')
axis('square')
axis off

Hf_5_deform_button = uicontrol(Hf_5 , 'Style' , 'pushbutton',
'Position', [20 60 130 20], 'String' , 'Deform');
```

```
 set(Hf_5_deform_button, 'Callback' , 'image_gaussian Deform')

 Hf_5_edit_box = uicontrol(Hf_5, 'Style' , 'edit', 'Position',[20
180 130 20]);


 case 'Deform'

  aa = str2double(get(Hf_5_edit_box, 'String'));

    c=128;
     w=waitbar(0,'Please Wait ...');
    for x_d=1:256
        waitbar(x_d/256);
    for y_d=1:256

        D = 1+exp(-(((x_d-128)^2 + (y_d-128)^2))/aa);
        D=1/D;
        O = [D 0; 0 D];
        A_S= inv(O) * ( [x_d;y_d]-[c;c])+[c;c];

        x_s=round(A_S(1));
        y_s=round(A_S(2));
        if x_s > 256 || x_s <=0
            x_s=1;
        end
        if y_s > 256 || y_s <=0
            y_s=1;
        end

        AI_G(x_d,y_d)=a(x_s,y_s);

    end
    end
close (w)
   figure , imshow(AI_G)

end % end function
```

ROI tracking subroutine

```
function image_stack(arg)
global Hf_6 Hf_6_edit_box_no_of_frames f
global a aa

a=im2double(a);
if nargin ==0
    arg='Initialize';
```

```
end
switch arg
     case 'Initialize'
Hf_6 = figure ('Position' , [300 90 400 400]);

Hf_6_edit_box_no_of_frames = uicontrol(Hf_6 , 'Style' , 'edit',
'Position' , [20 360 130 20]); %

Hf_6_text_above_box_no_of_frames = uicontrol(Hf_6 , 'Style' ,
'text', 'Position' , [20 380 130 20], 'String' , 'No. of frames',
'BackgroundColor', [0.8 0.8 0.8], 'FontSize', 10) ; % string,
written above edit box

Hf_6_get_frames_button = uicontrol(Hf_6 , 'Style' , 'pushbutton',
'Position', [20 320 130 20], 'String' , 'Get Frames', 'FontSize' ,
10);
set(Hf_6_get_frames_button, 'Callback' , 'image_stack Get_Frame')

% Hf_6_get_track_button = uicontrol(Hf_6 , 'Style' , 'pushbutton',
'Position', [20 280 130 20], 'String' , 'Track ROI', 'FontSize' ,
10);
% set(Hf_6_get_track_button, 'Callback' , 'image_stack Track_ROI')

case 'Get_Frame'
     no_of_frames = str2double(get(Hf_6_edit_box_no_of_frames,
'String'));
     for i=1:no_of_frames
         f = sprintf('Open File Number %d' , i);

         [filename , pathname]=uigetfile({'*.jpg','JPEG (*.jpg)'},
f); %
    file_string=strcat(pathname,filename);
    aa(:,:,i)=imread(file_string,'jpg');
    end % end for

        Hf_7 = figure ('Position' , [300 90 400 400]);
    for i=1:no_of_frames

    imshow((aa(:,:,i)),[]);
    F(i) = getframe;
end


movie(F,20)



end % end function
```

Subroutine called by ROI tracking subroutine

```
function [area_1 , area_image , centroid ] = area_con_2 (image)

% This function calculates area of chosen region
% It utilizes connectivity !

% Input = image
% output = area

% we need to convert input image to binary, then to label different
regions
image = im2double(image);
[labeled_image num]= bwlabel(im2bw(image));


% get ROI
%figure , imagesc(image) , axis('square')
%figure , imagesc((image)) , zoom on
%figure , imshow((image)) , zoom on
 imshow((image))
colormap(gray)
[x , y] = ginput(1);
x = round(x);
y = round(y);

value = labeled_image(y,x) ; % notice switching y and x
% value is the pixel intensity in the labeled_image. It is used
later for
% connectivity

%value
%num

[r,c] = find(labeled_image==value) ;

%r
%c

s = size(image) ; %s(1) is col or i ,,,, s(2) is row or j :-)

area_image = zeros(s(1),s(2));

s_r=size(r);


for i=1:s_r(1)
```

```
            area_image(r(i),c(i)) = 1;
end


%figure , imagesc(area_image)
area_1 = bwarea(area_image); % finding area

%% perimeter calculation
perim_image = bwperim(area_image);
%figure , imagesc(perim_image)
perimeter = bwarea(perim_image) ; % perimeter

% centroid
centroid = regionprops(bwlabel(area_image),'centroid');
centroid.Centroid(1);


oplot_image = ones(s(1), s(2));
oplot_image = oplot_image .* image;




figure , imshow(oplot_image)



colormap(gray)
hold on
for i=1:s_r(1)
y = r(i);
x=c(i);
fill([x x+1 x+1 x],[y y y+1 y+1],'r', 'LineStyle', 'none');
hold on
end
```

Subroutine called by ROI tracking subroutine

```
function [area_1 , area_image , centroid , perimeter] = track
(image,x,y)

% This function calculates area of chosen region
% It utilizes connectivity !

% Input = image
% output = area
```

```
% we need to convert input image to binary, then to label different
regions
image = im2double(image);
[labeled_image num]= bwlabel(im2bw(image));


% get ROI
%figure , imagesc(image)
%colormap(gray)
%[x , y] = ginput(1);
x = round(x);
y = round(y);


distance = 30;
value = labeled_image(y,x) ; % notice switching y and x

[r,c] = find(labeled_image==value) ;

%r
%c

s = size(image) ; %s(1) is col or i ,,,, s(2) is row or j :-)

area_image = zeros(s(1),s(2));

s_r=size(r);


for i=1:s_r(1)

            area_image(r(i),c(i)) = 1;
end


%figure , imagesc(area_image)
area_1 = bwarea(area_image) ;% finding area

%% perimeter calculation
perim_image = bwperim(area_image);
%figure , imagesc(perim_image)
perimeter = bwarea(perim_image) ; % perimeter

% centroid
centroid = regionprops(bwlabel(area_image),'centroid') ;
centroid.Centroid(1) ;
centroid.Centroid(2) ;

oplot_image = ones(s(1), s(2));
```

```
oplot_image = oplot_image .* image;


figure , imshow(oplot_image)




colormap(gray)
hold on
for i=1:s_r(1)
y = r(i);
x=c(i);
fill([x x+1 x+1 x],[y y y+1 y+1],'r', 'LineStyle', 'none');
hold on
end
```

References

1. **Haacke, E.M., *Magnetic resonance imaging : physical principles and sequence design*. 1999, New York: Wiley. xxvii, 914 p.**

2. **Kittel, C., *Quantum theory of solids*. 1963, New York,: Wiley. xi, 435 p.**

3. **Kittel, C., *Elementary statistical physics*. 1958, New York,: Wiley. 228 p.**

4. **Kraitchman, D.L., Sampath, S., Castillo, E., Derbyshire, J.A., Boston, R.C., Bluemke, D.A., Gerber, B.L., et al., *Quantitative ischemia detection during cardiac magnetic resonance stress testing by use of FastHARP.* Circulation, 2003. 107(15): p. 2025-30.**

5. **Osman, N.F., Kerwin, W.S., McVeigh, E.R., and Prince, J.L., *Cardiac motion tracking using CINE harmonic phase (HARP) magnetic resonance imaging.* Magn Reson Med, 1999. 42(6): p. 1048-60.**

6. **Osman, N.F., McVeigh, E.R., and Prince, J.L., *Imaging heart motion using harmonic phase MRI.* IEEE Trans Med Imaging, 2000. 19(3): p. 186-202.**

7. **Sampath, S., Derbyshire, J.A., Atalar, E., Osman, N.F., and Prince, J.L., *Real-time imaging of two-dimensional cardiac strain using a harmonic phase magnetic resonance imaging (HARP-MRI) pulse sequence.* Magn Reson Med, 2003. 50(1): p. 154-63.**

8. **Frangi, A.F., Niessen, W.J., and Viergever, M.A., *Three-dimensional modeling for functional analysis of cardiac images: a review.* IEEE Trans Med Imaging, 2001. 20(1): p. 2-25.**

9. **Dorri, F., Niederer, P.F., and Lunkenheimer, P.P., *A finite element model of the human left ventricular systole.* Comput Methods Biomech Biomed Engin, 2006. 9(5): p. 319-41.**

10. **Yun, K.L., Niczyporuk, M.A., Daughters, G.T., 2nd, Ingels, N.B., Jr., Stinson, E.B., Alderman, E.L., Hansen, D.E., et al., *Alterations in left ventricular diastolic twist mechanics during acute human cardiac allograft rejection.* Circulation, 1991. 83(3): p. 962-73.**

11. **Cerqueira, M.D., Weissman, N.J., Dilsizian, V., Jacobs, A.K., Kaul, S., Laskey, W.K., Pennell, D.J., et al., *Standardized myocardial segmentation and nomenclature for tomographic imaging of the heart: a statement for healthcare professionals from the Cardiac Imaging Committee of the***

Council on Clinical Cardiology of the American Heart Association. **Circulation, 2002. 105(4): p. 539-42.**

12. Liu, W., Ashford, M.W., Chen, J., Watkins, M.P., Williams, T.A., Wickline, S.A., and Yu, X., *MR tagging demonstrates quantitative differences in regional ventricular wall motion in mice, rats, and men.* Am J Physiol Heart Circ Physiol, 2006. 291(5): p. H2515-21.

13. Liu, W., Chen, J., Ji, S., Allen, J.S., Bayly, P.V., Wickline, S.A., and Yu, X., *Harmonic phase MR tagging for direct quantification of Lagrangian strain in rat hearts after myocardial infarction.* Magn Reson Med, 2004. 52(6): p. 1282-90.

14. Carroll, B.W. and Ostlie, D.A., *An introduction to modern astrophysics*. 1996, Reading, Mass.: Addison-Wesley Pub. 1 v. (various pagings).

15. Loganathan, R., Bilgen, M., Al-Hafez, B., Alenezy, M.D., and Smirnova, I.V., *Cardiac dysfunction in the diabetic rat: quantitative evaluation using high resolution magnetic resonance imaging.* Cardiovasc Diabetol, 2006. 5: p. 7.

16. Al-Shafei, A.I., Wise, R.G., Grace, A.A., Carpenter, T.A., Hall, L.D., and Huang, C.L., *MRI analysis of right ventricular function in normal and*

spontaneously hypertensive rats. **Magn Reson Imaging, 2001. 19(10): p. 1297-304.**

17. Al-Shafei, A.I., Wise, R.G., Gresham, G.A., Bronns, G., Carpenter, T.A., Hall, L.D., and Huang, C.L., *Non-invasive magnetic resonance imaging assessment of myocardial changes and the effects of angiotensin-converting enzyme inhibition in diabetic rats.* J Physiol, 2002. 538(Pt 2): p. 541-53.

18. Loganathan, R., Bilgen, M., Al-Hafez, B., Zhero, S.V., Alenezy, M.D., and Smirnova, I.V., *Exercise training improves cardiac performance in diabetes: in vivo demonstration with quantitative cine-MRI analyses.* J Appl Physiol, 2007. 102(2): p. 665-72.

19. Fang, Z.Y., Prins, J.B., and Marwick, T.H., *Diabetic cardiomyopathy: evidence, mechanisms, and therapeutic implications.* Endocr Rev, 2004. 25(4): p. 543-67.

20. Loganathan, R., Bilgen, M., Al-Hafez, B., and Smirnova, I.V., *Characterization of alterations in diabetic myocardial tissue using high resolution MRI.* Int J Cardiovasc Imaging, 2006. 22(1): p. 81-90.

21. Denney, T.S., Jr. and McVeigh, E.R., *Model-free reconstruction of three-dimensional myocardial strain from planar tagged MR images.* J Magn Reson Imaging, 1997. 7(5): p. 799-810.

22. Deng, X. and Denney, T.S., Jr., *Three-dimensional myocardial strain reconstruction from tagged MRI using a cylindrical B-spline model.* IEEE Trans Med Imaging, 2004. 23(7): p. 861-7.

23. O'Dell, W.G., Moore, C.C., Hunter, W.C., Zerhouni, E.A., and McVeigh, E.R., *Three-dimensional myocardial deformations: calculation with displacement field fitting to tagged MR images.* Radiology, 1995. 195(3): p. 829-35.

24. Bilgen, M. and Insana, M.F., *Error analysis in acoustic elastography. I. Displacement estimation.* J Acoust Soc Am, 1997. 101(2): p. 1139-46.

25. Bilgen, M. and Insana, M.F., *Elastostatics of a spherical inclusion in homogeneous biological media.* Phys Med Biol, 1998. 43(1): p. 1-20.

26. Bilgen, M., Srinivasan, S., Lachman, L.B., and Ophir, J., *Elastography imaging of small animal oncology models: a feasibility study.* Ultrasound Med Biol, 2003. 29(9): p. 1291-6.

27. **Adeghate, E., *Molecular and cellular basis of the aetiology and management of diabetic cardiomyopathy: a short review.* Mol Cell Biochem, 2004. 261(1-2): p. 187-91.**

28. **Ghiglia, D.C. and Pritt, M.D., *Two-dimensional phase unwrapping : theory, algorithms, and software*. 1998, New York: Wiley. xiv, 493 p.**

29. **Kellman, P., Aletras, A.H., Mancini, C., McVeigh, E.R., and Arai, A.E., *T2-prepared SSFP improves diagnostic confidence in edema imaging in acute myocardial infarction compared to turbo spin echo.* Magn Reson Med, 2007. 57(5): p. 891-7.**

30. **Koike, H., Watanabe, H., Inukai, A., Iijima, M., Mori, K., Hattori, N., and Sobue, G., *Myopathy in thiamine deficiency: analysis of a case.* J Neurol Sci, 2006. 249(2): p. 175-9.**

31. **Shabshin, N., Schweitzer, M.E., Morrison, W.B., Carrino, J.A., Keller, M.S., and Grissom, L.E., *High-signal T2 changes of the bone marrow of the foot and ankle in children: red marrow or traumatic changes?* Pediatr Radiol, 2006. 36(7): p. 670-6.**

32. **Stork, A., Muellerleile, K., Bansmann, P.M., Graessner, J., Kaul, M., Kemper, J., Adam, G., et al., *Value of T2-weighted, first-pass and delayed***

enhancement, and cine CMR to differentiate between acute and chronic myocardial infarction. **Eur Radiol, 2007. 17(3): p. 610-7.**

33. Takahashi, M., Uematsu, H., and Hatabu, H., *MR imaging at high magnetic fields.* Eur J Radiol, 2003. 46(1): p. 45-52.

34. De Roos, A., Kundel, H.L., Joseph, P.M., Doornbos, J., and Kressel, H.Y., *Variability of myocardial signal on magnetic resonance images.* Invest Radiol, 1990. 25(9): p. 1024-8.

35. Hanselman, D.C. and Littlefield, B., *Mastering MATLAB 7*. 2005, Upper Saddle River, NJ: Pearson/Prentice Hall. xi, 852.

36. Press, W.H., *Numerical recipes in fortran 77 : the art of scientific computing*. 2nd ed. 1996, Cambridge England ; New York: Cambridge University Press. xxxi, 933.

37. Saeed, M., Watzinger, N., Krombach, G.A., Lund, G.K., Wendland, M.F., Chujo, M., and Higgins, C.B., *Left ventricular remodeling after infarction: sequential MR imaging with oral nicorandil therapy in rat model.* Radiology, 2002. 224(3): p. 830-7.

38. **Young, A.A., Cowan, B.R., Thrupp, S.F., Hedley, W.J., and Dell'Italia, L.J., *Left ventricular mass and volume: fast calculation with guide-point modeling on MR images.* Radiology, 2000. 216(2): p. 597-602.**

39. **Young, A.A., Hunter, P.J., and Smaill, B.H., *Estimation of epicardial strain using the motions of coronary bifurcations in biplane cineangiography.* IEEE Trans Biomed Eng, 1992. 39(5): p. 526-31.**

40. **Young, A.A., Imai, H., Chang, C.N., and Axel, L., *Two-dimensional left ventricular deformation during systole using magnetic resonance imaging with spatial modulation of magnetization.* Circulation, 1994. 89(2): p. 740-52.**

41. **Gonzalez, R.C., Woods, R.E., and Eddins, S.L., *Digital Image processing using MATLAB*. 2004, Upper Saddle River, N. J.: Pearson Prentice Hall. xiv, 609.**